3D-printable chitosan/silk fibroin/cellulose nanoparticle scaffolds for bone regeneration *via* M2 macrophage polarization

Dinesh K. Patel [a,1], Sayan Deb Dutta [b,1], Jin Hexiu [c,1], Keya Ganguly [b], Ki-Taek Lim [a,b,*]

[a] *Institute of Forest Science, Kangwon National University, Chuncheon 24341, Republic of Korea*
[b] *Department of Biosystems Engineering, Kangwon National University, Chuncheon 24341, Republic of Korea*
[c] *School of Stomatology, Capital Medical University, Beijing 100050, China*

ARTICLE INFO

ABSTRACT

Biopolymers-induced immune microenvironment exhibited prominent effects on bone regeneration. Osteo-immunomodulatory responses of cellulose nanoparticles incorporated chitosan hydrogel scaffolds have not yet been reported. The objective of this study was to monitor the synergistic effects of silk fibroin and cellulose nanoparticles on the immune-modulatory behavior of chitosan biopolymer scaffolds. 3D-printed biodegradable cellulose nanoparticles-reinforced chitosan/silk fibroin (CS/SF/CNPs) scaffolds were fabricated and characterized by different spectroscopic techniques. The improved rheological and recovery strength was observed in CS/SF/CNPs hydrogels than pure polymer hydrogels. A significant shift from M1 → M2 macrophages polarization occurred in the CS/SF/CNPs scaffolds treated groups than the control after 3 days of incubation, showing its immune-modulatory potential. Osteo-immunomodulatory effects of the fabricated scaffolds were analyzed on human bone marrow-derived mesenchymal stem cells (hBMSCs), with macrophages-derived conditioned media (M-CM). Enhanced bone regeneration was observed in the calvaria defect rat model, indicating that the fabricated scaffolds are promising materials for bone-healing applications.

1. Introduction

Rapid regeneration of damaged tissue is one of the most significant challenges in tissue engineering (TE). The autogenous bone graft is considered an attractive therapeutic approach for treating defected bone. However, the lack of autogenous bone, extra surgical process, and possible risk of infection limit its broad applications (Zhou et al., 2021). The TE field has rapidly developed over the past few years to design and develop suitable constructs for damaged tissue (Amir Afshar & Ghaee, 2016). The 3D-printing technique has been widely utilized to construct the desired structures to accelerate tissue regeneration. Printed hydrogels are considered the promising materials for TE applications due to their resemblance in the extracellular matrix (ECM) of the native tissue, facilitating rapid cell proliferation and tissue regeneration (Zhang et al., 2018). The hydrogels should have the adequate mechanical strength to support the good adhesiveness between the neighboring layers for printing applications (Truby & Lewis, 2016). Mechanical strength, porosity, pore size, biocompatibility, and biodegradability of scaffolds are important parameters influencing their biomedical applications

(Hadisi, Nourmohammadi, & Mohammadi, 2015). Furthermore, it is also necessary to examine the body's immune response after the implantation of the scaffold materials. Immune cells, mainly, macrophages show inflammatory or anti-inflammatory responses after the implantation (Franz, Rammelt, Scharnweber, & Simon, 2011). These cells are accumulated at the implanted site and adhered with the implanted materials. They can combine and form giant cells. These cells secreted various chemical components to regulate their microenvironments, which play vital roles in tissue regeneration (Eming, Hammerschmidt, Krieg, & Roers, 2009; Vasconcelos et al., 2015). It has been observed that the biomaterials induced M2 macrophage polarization facilitated rapid bone regeneration (Wu et al., 2015). Biomaterials including, poly (glycolic acid) (PGA), poly (lactic acid) (PLA), poly (ethylene glycol) (PEG), poly (caprolactone) (PCL), collagen, alginate, fibroin, and chitosan, are widely used to develop scaffold for TE applications (Ambre et al., 2010; Hadisi et al., 2015; Li et al., 2015b; Zheng et al., 2014).

Chitosan (CS) has received substantial interest in developing scaffolds for biomedical applications because of its superior biocompatibility, biodegradability, and osteogenic potential (Liu, Zhang, Wu,

Xiong, & Zhou, 2012). The active functional groups, such as amine ($-NH_2$) and hydroxyl (–OH), provide an enormous opportunity to modify CS for various applications. However, the weak mechanical strength of CS restricts its broad applicability in load-bearing fields, thereby generating the need for the enhancement of its mechanical strength. Silk fibroin (SF) is a biopolymer considered a suitable polymer for fabricating composite biomaterials for biomedical applications. It has been observed that SF accelerates the wound healing process by promoting angiogenesis and cell proliferation (Osathanon et al., 2008). Therefore, incorporating SF in the CS matrix may generate better conditions for repairing the damaged tissues. Despite these advantages, SF has weak mechanical strength, restricting its exploitation as a biopolymer for high-performance applications (Dorishetty et al., 2020). This limitation can be overcome by incorporating suitable nanomaterials into its matrix. Nanocellulose, a natural polysaccharide, has received enormous attention for its use as a reinforcing agent due to its superior physicochemical properties (Lee, Aitomäki, Berglund, Oksman, & Bismarck, 2014). Depending on sources and structure, nanocellulose is further categorized as bacterial nanocellulose (BNC), cellulose nanofibrils (CNFs), and cellulose nanocrystals (CNCs)/cellulose nanoparticles (CNPs) (Patel, Dutta, & Lim, 2019). The high surface area and aspect ratio, superior mechanical strength, and excellent biocompatibility make CNPs a suitable material for use as a reinforcing agent to improve the polymer properties.

The bone regeneration potential of the nanocellulose-based biopolymer scaffolds has been earlier reported (Ferreira et al., 2019; Ingole et al., 2019; Rashad et al., 2018). Zhang et al. fabricated the aligned cellulose scaffolds loaded with growth factors for bone tissue engineering. An increased bone regeneration occurred in growth factor-loaded scaffolds than the unloaded scaffolds (Zhang et al., 2019b). However, the development of the scaffolds for rapid bone regeneration without using the growth factor is still a critical issue in TE.

To achieve this, we printed chitosan/silk fibroin/cellulose nanoparticles (CS/SF/CNPs) scaffolds using a bio-printer and evaluated their macrophage polarization and osteo-immunomodulatory responses with the murine-derived macrophage cell line Raw 264.7 (RAW) cells *in vitro*. This is the first study to show the macrophage polarization and osteo-immunomodulatory responses of Raw 264.7 cells with the 3D-printed CS/SF/CNPs scaffolds to the best of our knowledge. The scaffolds were characterized by Fourier transform infrared spectroscopy and X-ray diffraction analysis. The printed scaffolds exhibited superior swelling efficiencies. The upregulation of osteogenic-associated genes occurred in SF/CNPs-incorporated scaffolds *via* the mitogen-activated protein kinase (MAPK) pathway, showing their superior osteogenic potential. *In vivo,* the bone regeneration potential of the developed scaffolds was also evaluated in rats without using the growth factors. We hypothesize that the 3D-printed hydrogel scaffolds are multi-potentials and can be applied in bone tissue engineering.

2. Experimental section

2.1. Materials

All materials were used as received without further purifications. The high molecular weight chitosan powder (310–375 kDa, >75% deacetylated), potassium hydroxide (both from Sigma-Aldrich, St. Louis, MO, USA), sodium hydroxide (Junsei Chemicals, Tokyo, Japan), sodium chlorite, ammonium persulfate (Daejung Chemicals, Busan, Republic of Korea), and acetic acid (99.7%), and hydrochloric acid (35%) (mass/mass, Wako Chemicals, Osaka, Japan), were used in this experiment. Silk fibroin was purchased from Sigma-Aldrich, USA (~100 kDa).

2.2. Preparation of printable bio-ink

The bio-ink was prepared in 2% *v/v* acetic acid solution as previously described somewhere else (Kurian, Stevens, & McGrath, 2019). In brief,

the hydrogels were synthesized using chitosan (5% *w/v*), SF (1%), and CNPs (1%) (both *w/w*, w.r.t. CS) in the acetic acid solution. The air bubbles were removed from the developed bio-inks through centrifugation before the printing. Here, the pure chitosan, SF, and CNPs added printed scaffolds are indicated as CS, CS/SF, and CS/CNPs, respectively. The scaffold containing both SF and CNPs in the polymer matrix is considered as CS/SF/CNPs.

2.3. 3D-printing

The printing was performed using a CELLINK BIO-X printer (CELLINK Corporation, Sweden). A pre-designed structure was printed into the sterile plate keeping the printing bed temperature at 25 °C. The printing head temperature was kept at 35 °C. The structure was designed by the Solidworks software (www.solidworks.com, Dassault Biosystems, France). The rectangular ($20 \times 20 \times 2$ mm^3) structures were printed carefully into a sterile petri-disk using the 25G metal head needle (red color, blunt needle length: 6.35 mm, full length: 24.0 mm) with a printing speed of 3 mm/s. The printing pressure was in the range of 150–190 kPa. The uniformity factor (U) is calculated by using the following equation.

$$\text{Uniformaity factor (U)} = \frac{\text{Length of the printed strand}}{\text{Length of the theoretical design}}$$

The 3D-printed scaffolds were frozen at -80 °C for 24 h, followed by a lyophilization using a freeze dryer (EYELA® Freeze Drying Unit 2200, Tokyo, Japan) for 36 h to obtain the dry samples. After that, the scaffolds were immersed in 0.1 M sodium hydroxide solution for 10 min to neutralize it, followed by carefully washing with distilled water.

2.4. Characterizations

The functional groups in CNPs and their interaction with polymer chains were analyzed by the Perkin Elmer FTIR analyzer (Frontier, Perkin Elmer, UK) in the regions of 4000–400 cm^{-1} with 4 cm^{-1} resolution and 24 scans. The transmission electron microscopy (TEM) (JEM 2100 F, Jeol, Japan) was used to determine the size and morphology of the extracted CNPs. The X-ray diffractometer (X'Pert PRO MPD, Philips, Eindhoven, Netherlands) was used to monitor the structural changes in the polymer. The operating voltage and current were 40 kV and 40 mA, respectively, with Cu Kα radiation ($\lambda = 1.5414$ A°). The measuring range (2θ) was 5–40°. An ARES-G2 rheometer (TA Instruments, New Castle, Delaware, USA) was used to measure the mechanical and recovery strength of the synthesized hydrogels with a 6 mm parallel plate at 25 °C. The developed hydrogels were characterized by flow and temperature sweep.

2.5. Swelling study

The swelling efficiency of the developed scaffolds was evaluated in water at room temperature (25 °C) for different periods. Briefly, the known weights of the freeze-dried samples were dipped into water for a fixed time. After specific periods, the dipped samples were removed from the water. The excess water was removed from the surface of the scaffolds. For this, we did not press the scaffolds to release the water but softly contacted the surface of the scaffolds with tissue paper to remove the excess water. The weight of the scaffolds was measured and again placed in the same solvent. The swelling efficiency of the developed scaffolds was determined using the following equation.

$$\%\text{swelling} = \frac{W_s - W_d}{W_s} \times 100$$

Where, W_s and W_d are the weight of the soaked and dried scaffolds, respectively.

2.6. In vitro degradation

The degradation behavior of the developed scaffolds was analyzed in the PBS (0.2 M), and the protease solutions as previously reported somewhere else with some modifications at room temperature (25 °C) (Wan, Wu, Cao, & Dalai, 2008). The enzyme concentration was taken at 1 mg/mL in this study. For this, the known amounts of the scaffolds were dipped into the PBS and protease solutions for a fixed period. After that, the scaffolds were taken from the media (PBS and protease) and washed with distilled water. The excess water was removed with the tissue paper. The scaffolds were dried, and weights were measured. The protease solution was changed after 3 days period. The *in vitro* degradation was calculated using the following equation.

$$\text{Weight loss (\%)} = \frac{W_i - W_d}{W_i} \times 100$$

Where, W_i and W_d are the weight of the initial and degraded scaffolds, respectively.

2.7. Cell viability

Cytotoxicity of the developed scaffolds was analyzed *via* WST-1 assay (EZ-Cytox Cell Viability Assay Kit®; DoGenBio Co., Ltd., Republic of Korea) in the presence of hBMSCs. For that, 1×10^4 cells were placed onto the surface of the scaffolds in 96-well plates and incubated at 37 °C for different periods. The groups without the scaffolds were considered as control. After the incubation, the old media were changed with pure media, and WST-1 dye was added to each well and further incubated for 2 h to form formazan. The formed formazan was collected in a separate 96-well plate to take the absorbance. A spectrophotometer (Infinite® M Nano 200 Pro; TECAN, Switzerland) was used to measure the formazan concentrations by taking the absorbance at 450 nm. All experiments were performed in triplicate ($n = 3$), and data are presented at mean ODs ± standard deviations (SD). Statistical significance was taken at $^*p < 0.05$.

2.8. Cell morphology

The morphologies of the cultured hBMSCs were examined through an inverted fluorescence microscope (DMi8 Series, Leica Microsystems, Germany). Briefly, 1×10^4 cells were incubated with or without the printed scaffolds for four days. The groups without the sample were to be considered as control. After that, the cells were washed with PBS and fixed by 4% paraformaldehyde (PFA) solution (Sigma-Aldrich, USA). The fixed cells were permeabilized with 0.1% Triton-X 100 for 10 min, followed by blocking with 1% bovine serum albumin (BSA) (Sigma-Aldrich, USA) for 60 min. The cells were treated with 200 μL of Alexa Fluor 488-conjugated Phalloidin (F-Actin Probe) (Invitrogen, Thermo Fisher Scientific, USA) for 20 min. The nuclei were stained with 4, 6-diamino-2-phenylindole dihydrochloride (DAPI) (Sigma-Aldrich, USA) for 5 min. The excess stains were removed with PBS washing, followed by the mounting with a small amount of (1 drop) of Prolong® Antifade mounting media (Invitrogen, Thermo-Fischer Scientific, USA). The morphologies were taken using suitable filter channels.

2.9. Alkaline phosphatase (ALP) activity and mineralization

ALP activity of the printed scaffold was assessed in hBMSCs by the amplite colorimetric alkaline phosphatase assay kit (AAT Bioquest, Sunnyvale, CA, USA) as per the manufacturer's protocols after 7 and 14 days of treatment. For this, cells (4×10^4) were cultured in a 24-well plate with and without the scaffolds. The groups without scaffolds treatment were considered as control. After that, the cultured media (50 μL) were collected from the plate and treated with 50 μL of para-nitrophenyl phosphatase (p-NPP) and incubated at 37 °C for 30 min. The absorbance was measured by a spectrophotometer at 400 nm. ALP

values were determined by the standard curve.

The mineralization potential of the developed scaffolds was evaluated by the alizarin red staining (ARS) technique in hBMSCs after 7 and 14 days of treatment, as previously reported somewhere else (Patel et al., 2021a). The groups without any treatment were considered as control. For this, 4×10^4 cells were taken in 24-well plates and incubated for the desired periods. The old osteogenic media were replaced with pure osteogenic media every 3 days. After that, cells were washed with PBS solution and fixed with 4% PFA solution for 15 min at room temperature. The fixed cells were washed with distilled water, followed by staining with 40 mM ARS (pH 4.2) solution. The stained cells were left for 30 min. The washing of the stained cells was performed with distilled water. The mineralization images were captured using an optical microscope (Zeiss Optical Microscope, USA). After that, the stained cells were treated with the de-staining solution to quantify the formed minerals. The staining solution has consisted of 10% of cetylpyridinium chloride and 10 nM of sodium phosphate (Sigma-Aldrich, USA). The absorbance was taken at 562 nm through a spectrophotometer. All measurements were performed in triplicate ($n = 3$), and results are shown as mean OD ± standard deviation (SD). Statistical significance was considered at $^*p < 0.05$.

2.10. RNA extraction and real-time polymerase chain reaction analysis

The osteogenic-associated gene expression in hBMSCs with the scaffolds was measured by the real-time polymerase chain reaction (q-PCR) technique after 7 and 14 days of incubation. The groups without scaffolds treatment were taken as control. For this, 4×10^4 cells were incubated in 24 well-plates with osteogenic differentiation media in 5% CO_2 incubator at 37 °C for the required periods. The RNA extraction was performed with TRIzol reagent (Thermo Fischer Scientific, USA) as per the manufacturer's guidelines. The purity and concentration of the isolated RNA were determined using a spectrophotometer. The synthesis of cDNA was done with reverse transcriptase (Superscript II RTase; Invitrogen, Gaithersburg, MD) and SYBR Green Master Mix (Bio-Rad, USA). The mRNA expression was monitored by the Bio-Rad Real-Time PCR (CFX96™ Maestro Real-Time Systems, Bio-Rad, USA) instrument. The experimental conditions were involved denaturation (43 cycles) at 95 °C for 15 s and amplification at 60 °C for 1 min. All experiments were done in triplicate ($n = 3$), and normalized with the housekeeping gene hypoxanthine-guanine phosphoribosyl transferase (*HPRT*). The relative expression of mRNA in hBMSCs with scaffolds and control was compared in a histogram. The primer sets applied in this experiment are mentioned in Table S1.

2.11. Immunocytochemical staining

The expression of osteogenic-associated protein markers in hBMSCs was investigated using immunofluorescence (IF) and immunohistochemistry (IHC) techniques. For this, cells (2.5×10^4) were incubated with or without the scaffolds for 7 days in the osteogenic differentiation media. The groups without the scaffolds were considered as control. After incubation, cells were rinsed with PBS and fixed with 4% PFA solution at room temperature for 15 min, followed by the permeabilization with absolute methanol for 10 min. The permeabilized cells were blocked with 1% BSA solution for 1 h, followed by the incubation with the specific antibodies against Runx2, ALP, and OPN at 4 °C for 12 h. After that, incubation with secondary antibodies (AF-488, and AF-594) was performed for 1 h, followed by the washing and staining with PBS and DAPI at room temperature, respectively. Photographs of the stained cells were captured by an inverted fluorescence microscope at 40× magnification. All antibodies were purchased from the Santa Cruz Biotechnology (SCBT), California, USA.

For IHC analysis, the PFA-fixed cells were treated with 30% (*v/v*) H_2O_2 solution to block the endogenous peroxidases. After that, cells were treated with the specific primary and secondary antibodies and

stained with DUB substrate kit (ab64238, Abcam, USA) at room temperature for 10 min, followed by the staining with the Harris' Hematoxylin solution for 1 min. The stained cells were washed with PBS and the images were captured by an optical microscope. The expression of Runx2, ALP, and OPN markers was quantified using ImageJ software (ImageJ, v1.8, NIH, Bethesda, USA) with Fiji plugins, as earlier reported (Baek et al., 2021). The details of the used specific antibodies are given in Table S2.

2.12. Cytokine array

The cytokine expression and MAPK signaling pathway in hBMSCs were evaluated by the Raybiotech Human Antibody Array kit (Raybiotech, USA) as per the manufacturer's protocols. In brief, cells were cultured with or without the scaffolds in the serum-free DMEM media for 24 h. The secreted media (supernatants from cells) were collected and used for the cytokine array.

For MAPK signaling pathway analysis, the serum-deprived cells were lysed with the radioimmunopercipitation assay (RIPA) buffer containing protease and phosphatase inhibitors. The lysed protein was collected and used for the MAPK signaling array. The membranes were developed using a specific detection solution, and the spots were identified by the chemiluminescence detection device (ChemiDoc XRS+ System, Bio-Rad, USA). Densitometry was completed with ImageJ software, and data are represented as mean ± SD of triplicate ($n = 3$) experiments (Liu, Li, Xu, Zheng, & Cao, 2018).
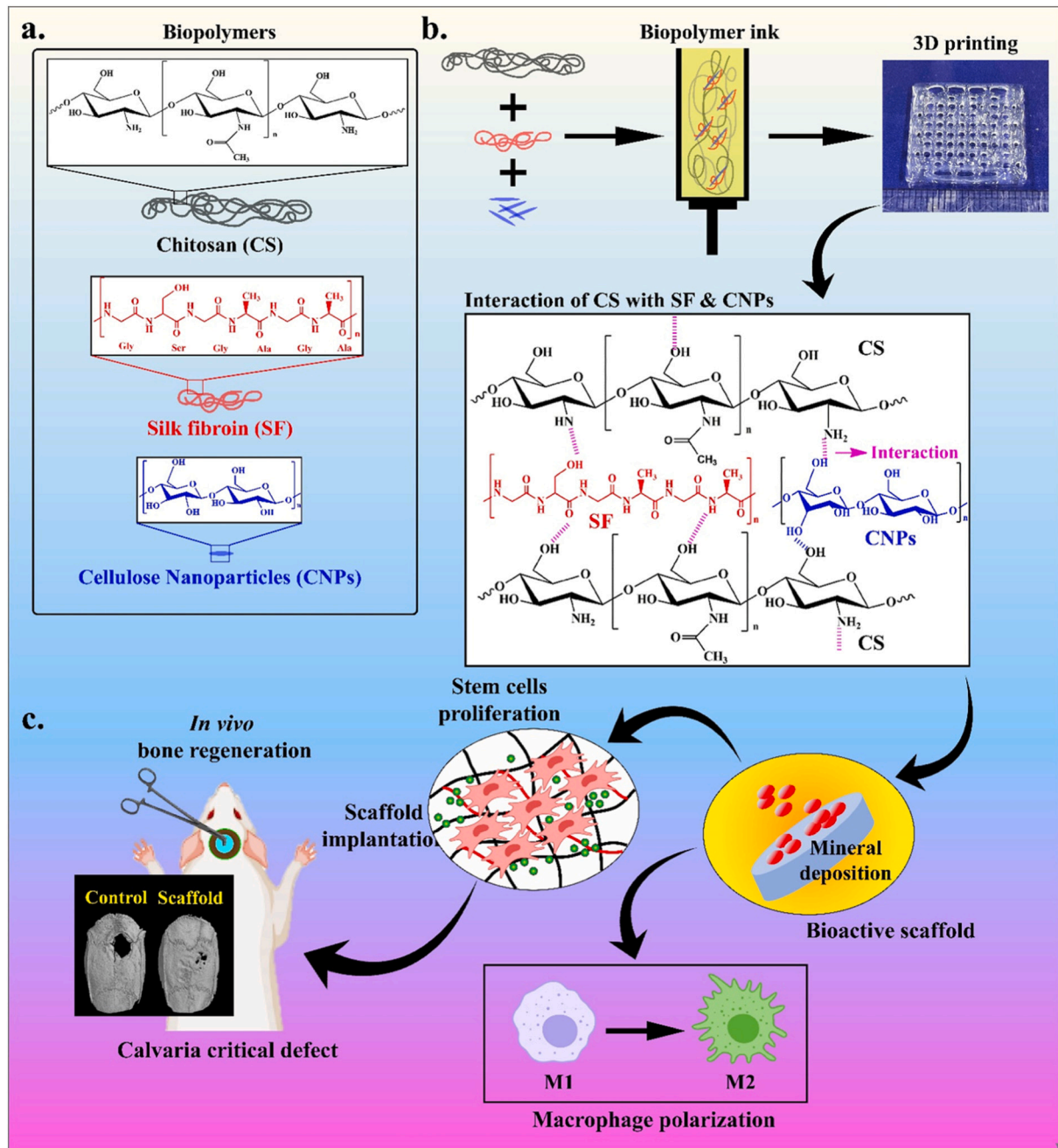

Fig. 1. Schematic presentation for the fabrication of chitosan/silk fibroin/cellulose nanoparticles (CS/SF/CNPs) hydrogel, (a) The chemical structure of the used components, (b) Fabrication steps and possible interactions between the incorporated components, and (c) Enhanced cellular activity and improved bone regeneration application of the printed scaffolds.
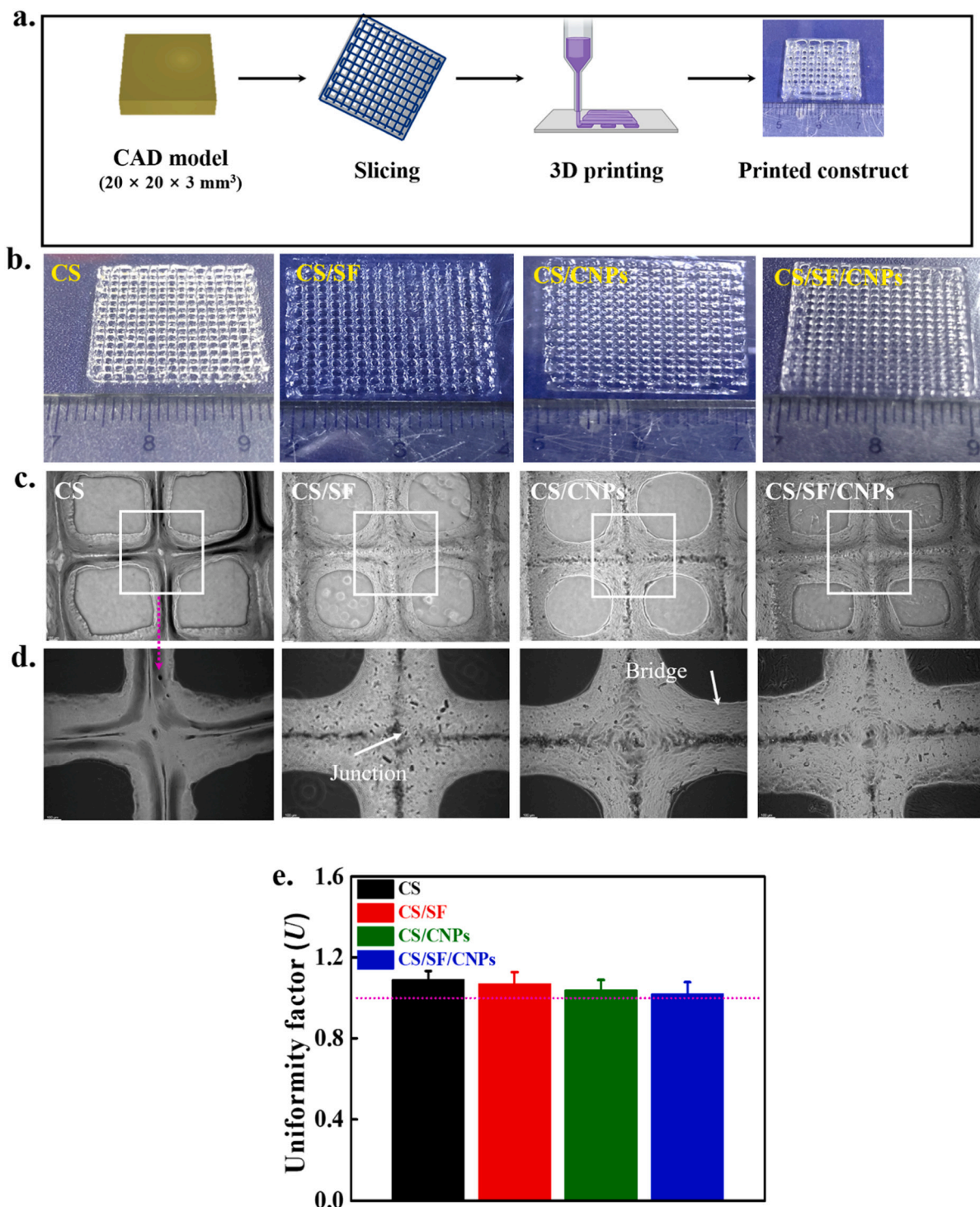
Fig. 2. (a) Schematic presentation for the designing of 3D construct from CAD program, (b) Photographs of the printed scaffolds, (c) Light microscopic images of the printed scaffolds, (d) The magnified images of the highlighted area of the printed scaffolds with junction and bridge, and (e) Uniformity factor (U) of the printed scaffolds.

2.13. Macrophage polarization study

The culture process for Raw 246.7 cells is given in Supplementary Information. The biocompatibility of the fabricated scaffolds was also measured with Raw 246.7 cells by WST-1 technique. For this, 1×10^4 cells were plated in 96 well plates and incubated with and without scaffolds for 1, 3, and 5 days. The old media were replaced with pure media after 3 days. After incubation, WST-1 dye was added, and

absorbance was measured at 450 nm by a spectrophotometer.

The conditioned media were developed as previously reported somewhere else (Zhong et al., 2021). In brief, 1×10^4 Raw 264.7 cells were treated with the fabricated scaffolds in 24 well-plate for 24 h in 5% CO_2 incubator. After that, the supernatant was taken out and centrifuged at 3000 rpm for 15 min. The obtained supernatant media were labeled as macrophage conditioned media (M-CM) and stored at 4 °C for further applications.

The expression of different macrophage-related gene markers (CD68, iNOS, CD86, and CD163) was studied in Raw 264.7 cells by the FACS technique after 24 and 72 h of incubation as per manufactures guidelines. Briefly, 4×10^4 cells were treated with the scaffolds for the desired periods. The groups without any treatment were assumed as control. The dilution of primary and secondary antibodies was 1:250, and 1:150, respectively.

The expression of macrophage-related gene markers (CD68, iNOS, CD86, and CD163) in Raw 264.7 cells was also monitored by the immunofluorescence (IF) technique after 3 days of incubation. In brief, cells (2.5×10^4) were incubated with or without the scaffolds for the desired periods in DMEM media. The groups without the scaffolds were taken as control. After treatment, cells were rinsed with PBS and fixed with 4% PFA solution at room temperature for 15 min. The fixed cells were treated with absolute methanol for 10 min, followed by blocking with 1% BSA solution for 1 h. The blocked cells were incubated with the specific antibodies against CD68, iNOS, CD86, and CD163 at 4 °C for 12 h. Furthermore, incubation with secondary antibodies (AF-555, and FITC) was accomplished for 1 h. The incubated cells were rinsed with PBS and stained by DAPI at room temperature. The fluorescence morphologies of the stained cells were taken by using an inverted fluorescence microscope. All antibodies for immunofluorescence (IF) technique and FACS analysis were purchased from the SCBT, Inc. California, USA.

The osteo-immunomodulation effects of the M-CM were assessed with hBMSCs by the ARS technique after 24 h of treatment. For this, 4×10^4 hBMSCs were treated with different scaffolds in the presence of 100 μL M-CM for the desired periods. After that, cells were washed with PBS solution and fixed with 4% PFA solution for 15 min at room temperature. The fixed cells were rinsed with distilled water, followed by staining with 40 mM ARS (pH 4.2) solution for 30 min. The washing of the stained cells was performed with distilled water. The mineralization images were captured using a fluorescence microscope.

The migration study was performed to examine the wound healing potential of hBMSCs in the M-CM with or without the scaffolds for 6 and 24 h as earlier reported somewhere else (Dutta et al., 2021). In brief, cells were cultured in 6-well plates till the confluency (~90%). After that, the wound area was made by a plastic tip (1 mm), and washed with PBS to eradicate the cellular debris. The cell migration images were captured by an optical microscope after 6 and 24 h of treatment.

2.14. In vivo study

2.14.1. Animal care and maintenance

In vivo bone regeneration analysis was performed with two-month-old ICR male rats ($N = 12$). All surgical protocols were approved by the Capital Medical University Animal Experimental Ethics Committee (AEEC, Institute of Animal Care and Use Committee of Capital Medical University, Permission No. CMUSH-IRB-KJ-YJ-2020-29). *In vivo* experiments were divided into four groups, each group having three rats ($n = 3$). The rats ($n = 3$) without any treatment were taken as the control. The CS, CS/CNPs, and CS/SF/CNPs scaffolds treated rats (in each group, $n = 3$) were considered as experimental groups, respectively. All animals were kept in an insulated and sound-proof room. The room temperature was maintained at 21 ± 2 °C with a constant relative humidity (RH) of 35 ± 2%. The room was adjusted with the automatically controlled 12 h light and 12 h dark cycle. All possible efforts were taken to reduce animal suffering and minimize the number of animals required to generate reliable scientific results. The scaffolds were sterilized before the implantation.

2.14.2. Animal surgery and implantation of scaffolds

All rats were anesthetized with 5% pentobarbital sodium (Sigma-Aldrich, USA) at 0.5 mL/kg before surgery. After that, the sagittal incisions (1–1.5 cm) were cautiously created on the scale with the sterile surgical blade. Approximately 5 mm critical defect was made in the central area of the calvaria bone under continuous washing with sterile

1% saline. The interesting area was washed carefully by a surgical gauge. After that, the defect area was transplanted with 5 mm × 5 mm circular scaffolds for 5 weeks. After transplantation, the soft tissues were repositioned and sutured. All animals were permitted free access to food and water until sacrifice.

2.15. Statistical analysis

Statistical analyses were accomplished with one-way ANOVA from OriginPro 9.0 software. All results were presented as mean $\pm$ SDs. Statistical analysis was performed between the control and treated groups. Statistical significance was considered at $^*p < 0.05$, $^{**}p < 0.01$, and $^{***}p < 0.001$.

3. Results and discussion

3.1. 3D-printing of scaffolds

A schematic presentation for the formation of the hydrogel scaffolds and their applications is shown in (Fig. 1).

The detailed spectroscopic characterizations (FTIR and AFM) of pure cellulose and CNPs are provided in (Fig. S1a–c). The hydrogel formed a thread-like structure during the printing, which is necessary for printing applications. The formation of the thread-like structure is given in (Fig. S2a). The easy extrusion of the hydrogel from the needle indicates the shear-thinning behavior of the developed hydrogel. A photograph of the 3D-printed scaffold during the printing is shown in (Fig. S2b). The printed structure retains its pre-designed morphology, indicating that re-solidification occurred reasonably after the printing. The important criteria for printing are the extrusion of printing bio-ink from the nozzle, transition of solid-like property into liquid, and re-solidification (Zhang et al., 2018). Additionally, re-solidification should occur at an appropriate rate to maintain the adhesiveness behavior between the printed layers. The rapid re-solidification can cause poor adhesion between the printed layers. A schematic presentation for the 3D-printing construct is given in (Fig. 2a). The construct was designed by the computer-aided design (CAD) program. The 3D-printed structures from the developed hydrogels are presented in (Fig. 2b). The space between the layers was retained in the printed structures suggested good adhesion between layers during the printing without using any cross-linking agents. The dimensional accuracy and the mechanical strength of the 3D-printed scaffolds are profoundly affected by several parameters, including instrument parameters, physicochemical properties of the materials, and the design of the scaffolds for the printing (Asadi-Eydivand, Solati-Hashjin, Farzad, & Abu Osman, 2016). It is necessary to assess the dimensional accuracy and mechanical strength of the printed porous scaffolds for bone tissue engineering. We examined the physical-mechanical strength of the 3D-printed scaffolds by twisting their structures, and the images are shown in (Fig. S2c). The printed structures retained their morphology in different conditions, indicating their stability, required in tissue engineering applications (Derakhshanfar et al., 2018). The optical microscopy images of the printed scaffolds are shown in (Fig. 2c–d). The bridge and junction parts are clearly visible without any collapse of the printed layers in the structure. The orientation of the material is also visualized, which is directed towards the printing direction. The uniformity factor (U) of the printed scaffolds was measured to validate the printing conditions, and results are presented in (Fig. 2e). The U value was 1.09, 1.07, 1.04, and 1.02 for CS, CS/SF, CS/CNPs, and CS/SF/CNPs, respectively. The U value for the composite hydrogels was approximately one compared to the pure polymer hydrogel, showing that the developed hydrogels are suitable for printing applications. Different factors, such as adhesion of bio-ink during printing, deformation caused by gravity, non-uniform extrusion of the bio-ink, viscosity, shear-thinning, and thixotropic properties of the bio-ink play significant roles in the uniformity of the printed scaffolds (Gao et al., 2018; He et al., 2016). The bio-inks with low viscosity and thixotropic properties
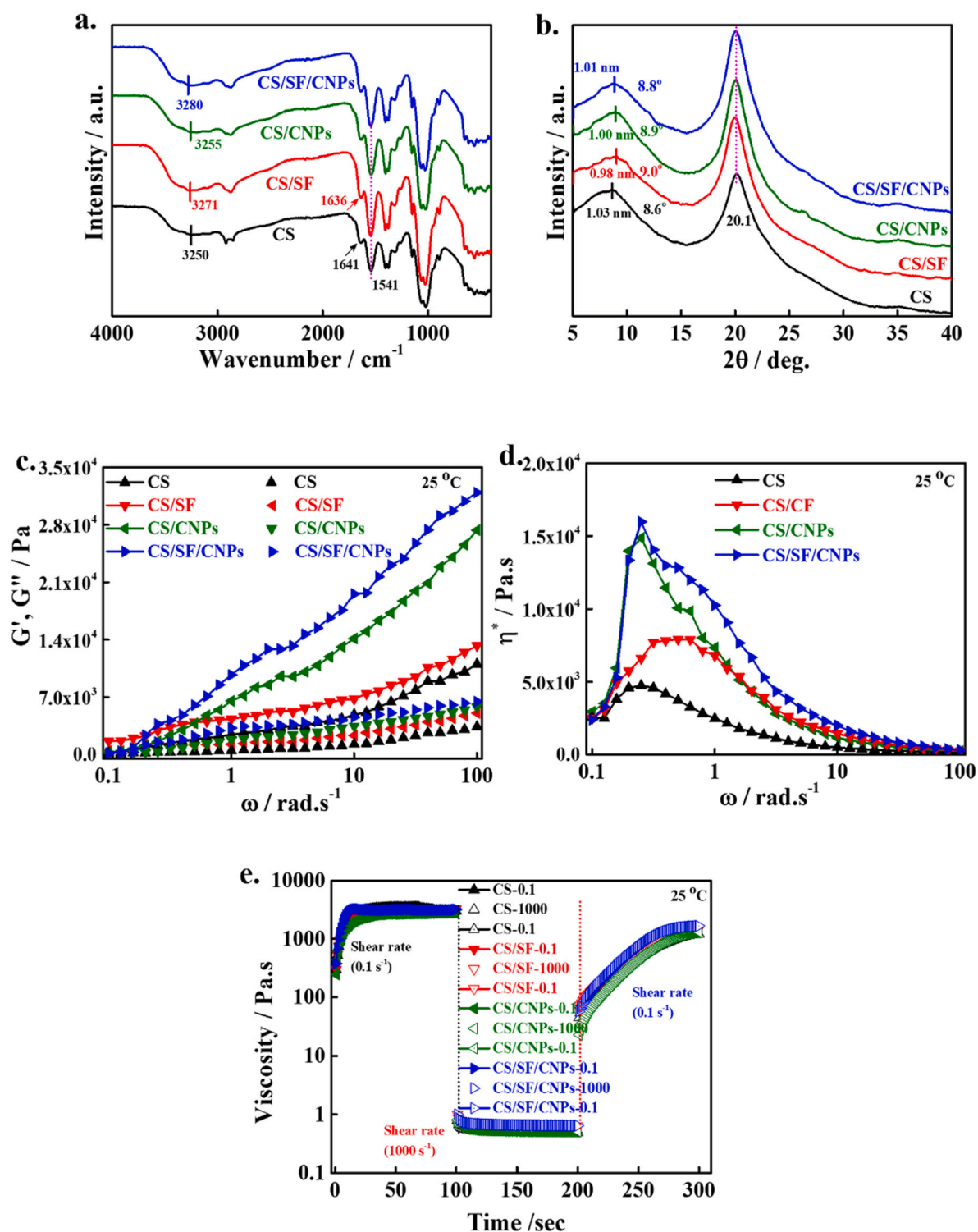
Fig. 3. Spectroscopic characterizations of the scaffolds, (a) FTIR spectra, (b) XRD patterns of the indicated scaffolds, (c) The storage modulus (G′, solid lines) and loss modulus (G″, without lines) values of the synthesized hydrogels in the angular frequency (ω) ranges of 0.1–100 rad/s, (d) Corresponding viscosity complex (η*) of the developed hydrogels in the angular frequency (ω) ranges of 0.1–100 rad/s, and (e) Evaluation of the recovery strength of the prepared hydrogel for bone tissue engineering.

have a higher chance of deviation from the uniformity. The CS hydrogel has comparatively low viscosity, and thixotropic properties than other hydrogels exhibited slightly higher U value than the others. Among these (CS, CS/SF, CS/CNPs, and CS/SF/CNPs), CS/SF/CNPs hydrogel exhibited improved viscosity, and thixotropic properties made them ideal for uniform printing.

The SEM morphologies of the printed scaffolds after the freeze-drying are given in (Fig. S3). The CS/SF/CNPs scaffold shows a more rough structure than the other printed scaffolds, favoring better cellular activity (Mitra, Tripathi, Sharma, & Basu, 2013). Furthermore, the layered structures were also visible in the printed structures, showing the good adhesiveness of the printed layers.
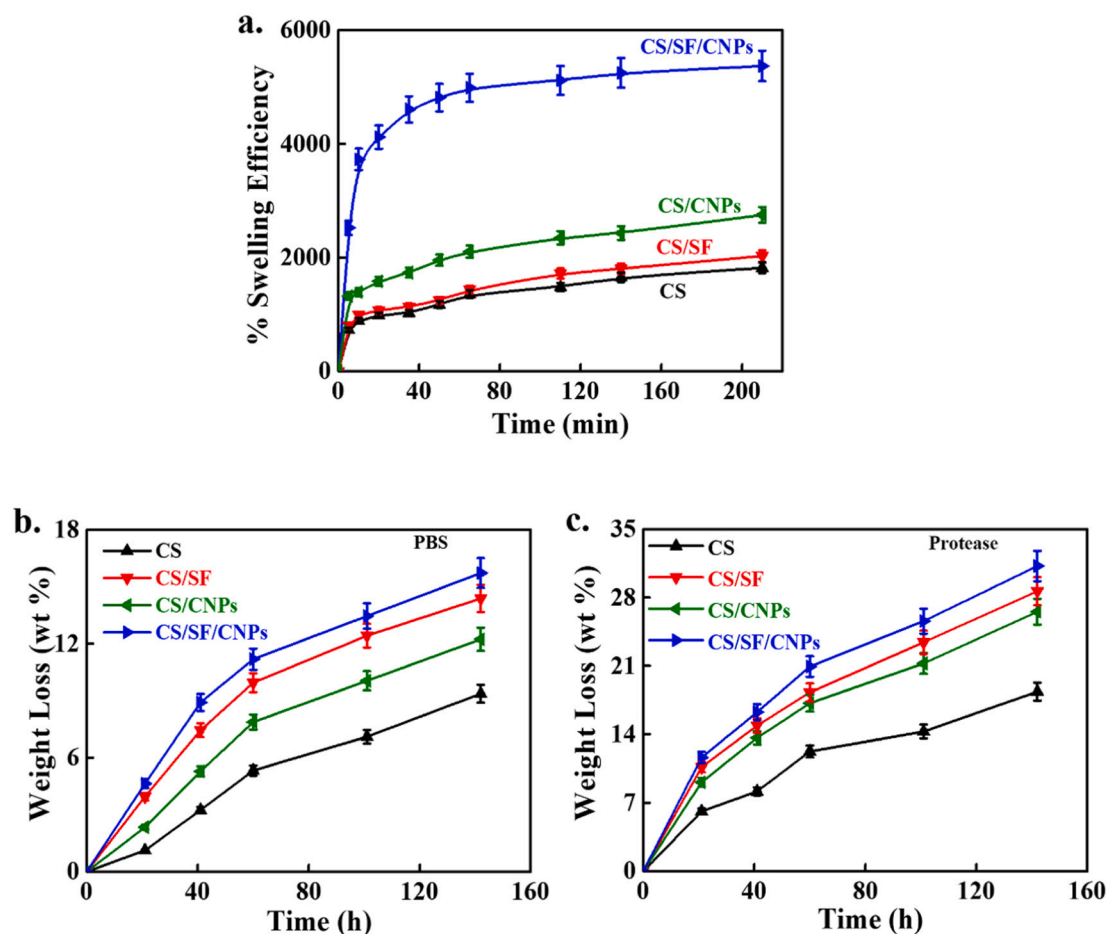
Fig. 4. (a) Determination of the swelling potential of the fabricated scaffolds in the water at room temperature, (b) The degradation rate of the developed scaffolds in the PBS media, and (c) in the protease media.

3.2. Spectroscopic analysis and recovery behavior

The FTIR spectra of the printed scaffolds are shown in (Fig. 3a). The pure chitosan scaffold exhibits a broad absorption peak in the region of 3250 cm^{-1}, indicating the presence of amine and hydroxyl functional groups in the structure, which further shifted towards higher wavenumbers ($3250 \rightarrow 3280 \text{ cm}^{-1}$). This shift in the composite scaffolds was attributed to the insertion of filler moieties within the polymer chains, caused a decrease in intramolecular hydrogen bonding interactions between the pure polymer chains, and increased the intermolecular hydrogen bonding interactions between the polymer chains and filler. The FTIR absorption peaks in the pure chitosan at 1641 and 1541 cm^{-1} were due to the carbonyl ($>$C$=$O) stretching of the amide I peak and bending vibration of $>$N—H for *N*-acetylated moieties, respectively (Patel et al., 2021b). A shift in the $>$C$=$O peak ($1641 \rightarrow 1636 \text{ cm}^{-1}$) was observed in the composite scaffolds because of the interaction between the polymer chains and added filler. However, no significant change was observed in the bending vibration of $>$N—H for the *N*-acetylated moieties in the composite scaffolds.

The influence of the incorporated filler on the structural changes in the pure polymer was examined using an X-ray diffractometer, and the results are shown in (Fig. 3b). The pure chitosan sample exhibited broad and sharp diffraction peaks at 8.6° and 20.1° for the amorphous and crystalline regions, respectively. The incorporated filler did not affect the crystalline peak of the chitosan, whereas a slight decrease in the interplanar distance was observed in the amorphous regions, suggesting the insertion of the filler predominantly occurred in amorphous regions. The insertion of the filler within the polymer chains is responsible for the

decrease in the interplanar distance and increased interaction between the filler and polymer chains, as observed in the FTIR data (Jin et al., 2013).

The rheological strength of the developed hydrogels was evaluated using a rheometer at 25 °C to assess the strength of the cross-linked network structures within the hydrogels. The storage modulus (G′) and loss modulus (G″) values of the developed hydrogels in the angular frequency (ω) ranges of 0.1–100 rad/s are given in (Fig. 3c). The composite scaffolds exhibited greater G values (solid lines) than the pure polymer hydrogel. This enhancement is attributed to the strong interaction between the polymer chains and incorporated filler, causing the generation of interconnected network structures, which restrict the motion of the polymer chains and, consequently, increase the G values in composite hydrogels compared to that observed in the pure polymer hydrogel (Patel et al., 2021c; Yang, Bakaic, Hoare, & Cranston, 2013). Approximately 3 times ($1.1 \times 10^4 \rightarrow 3.1 \times 10^4$ Pa) enhancement in the G′ values were observed in CS/SF/CNPs hydrogel compared to the CS hydrogel at the higher frequency region. This is probably due to the greater relaxation and motion of the polymer chains at a higher angular frequency, facilitating the formation of a more cross-linked morphological structure, thereby enhancing the elasticity of the fabricated hydrogels (Pati et al., 2014; Yang et al., 2013). The composite hydrogels showed a greater G″ (without lines) value vis-à-vis that of pure polymer hydrogel, and among these (CS/SF, CS/CNPs, and CS/SF/CNPs composite hydrogels), CS/SF/CNPs exhibited higher G″ values. However, the magnitude of G″ was low compared to that of G′ throughout the measured range, owing to the formation of a cross-linked structure. The higher G′ value compared to that of G″ indicates that the developed
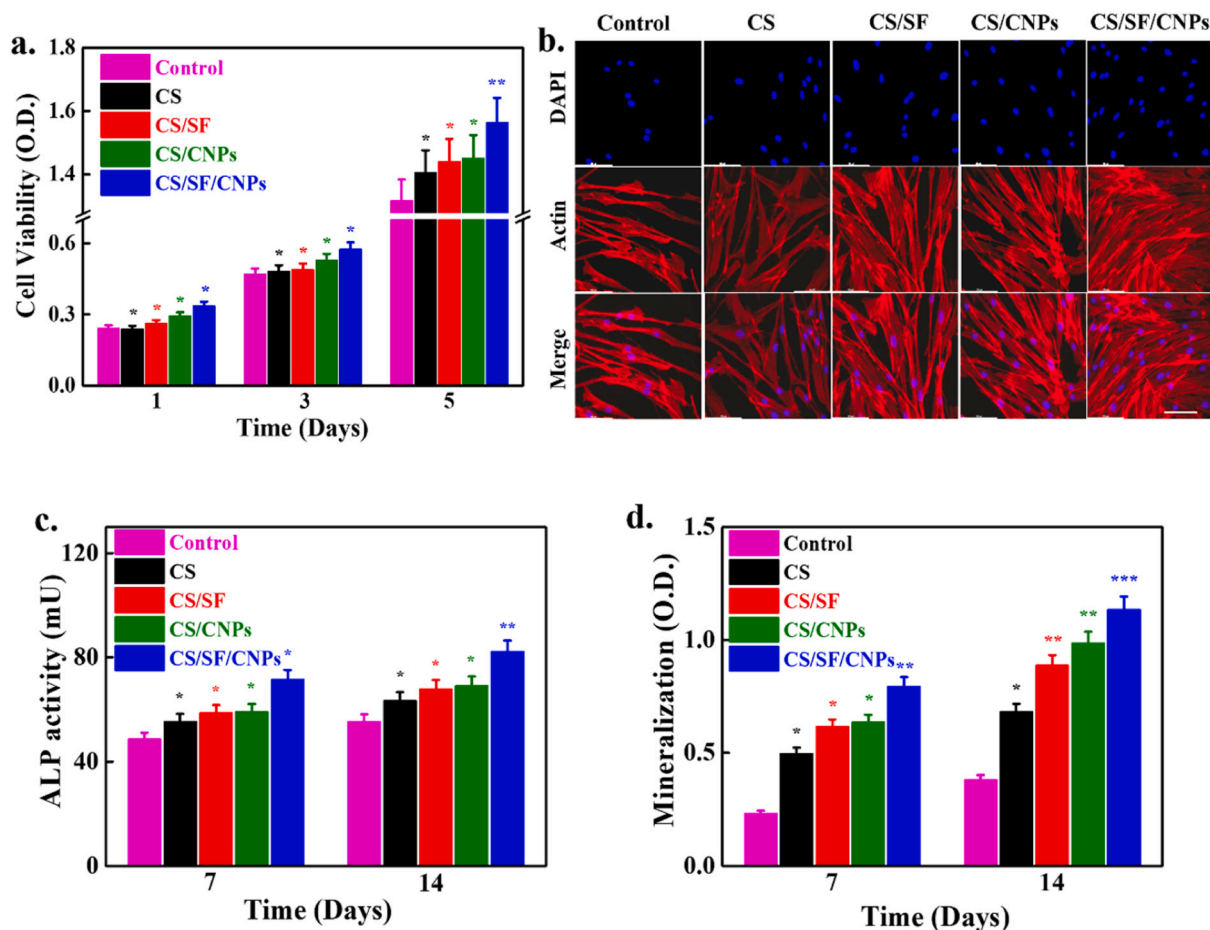
Fig. 5. Cytotoxicity evaluation of the printed scaffolds in the presence of hBMSCs at different time periods, (a) Cell viability of hBMSCs in the presence of developed scaffolds at indicated time periods, (b) Fluorescence morphologies of hBMSCs in the presence of indicated scaffolds after 4 days of treatment. (c) ALP activity of the fabricated scaffolds in the presence of hBMSCs after 7 and 14 days of treatment, and (d) Mineralization potential of the fabricated scaffolds in the presence of hBMSCs after 7 and 14 days of treatment ($^{*}p < 0.05$, $^{**}p < 0.01$, and $^{***}p < 0.001$).

hydrogels were elastic.

The changes in the viscosity complex (η^*) of the developed hydrogels in the angular frequency (ω) range of 0.1–100 rad/s are shown in (Fig. 3d). The composite hydrogels demonstrated greater η^* values than the pure polymer hydrogel because of the formation of cross-linked structures via greater interaction. An enhancement in the η^* value was also reported in alginate/chitosan hydrogel, increasing the chitosan contents in the alginate matrix due to the formation of cross-linked structures through the interactions (Liu et al., 2018). Higher η^* values were observed at a low frequency, which was further decreased by increasing the magnitude of the measuring frequency, showing the shear thickening and shear thinning properties. Therefore, it is possible to tune the mechanical strength of chitosan by adding an appropriate combination of fillers.

The recovery strength of the developed hydrogels was analyzed by measuring the viscosity in different conditions. The analysis was performed in a low shear rate (0.1 s^{-1}) for 100 s, followed by a high shear rate (1000 s^{-1}) for 100 s to check the deformations in the developed hydrogels. Finally, the shear rate was suddenly decreased to the initial condition (0.1 s^{-1}) and measured the viscosity of the hydrogels for another 100 s. The changes in the viscosity of the developed hydrogels under different treatment conditions are demonstrated in (Fig. 3e). The developed hydrogels should have the thixotropic property for printing applications, which means that the viscosity of the hydrogels should decrease under a high shear condition and swiftly recover by removing the high shear conditions (Abouzeid et al., 2018). The initial viscosity was 3004.49, 3256.0, 2844.01, and 3204.62 Pa.s after 100 s of

treatment, which suddenly decreased to 0.4994, 0.6384, 0.5106, and 0.6423 Pa.s for CS, CS/SF, CS/CNPs, and CS/SF/CNPs, respectively, under high shear conditions. A significant enhancement in the viscosity was observed after the removal of the high shear rate, and the obtained values were 1217.6, 1463.87, 1301.02, and 1663.54 Pa.s for CS, CS/SF, CS/CNPs, and CS/SF/CNPs, respectively, showing the thixotropic property of in the developed hydrogels. The recovery strength was 40.5, 44.93, 45.72, and 51.9% for CS, CS/SF, CS/CNPs, and CS/SF/CNPs, respectively. This enhancement in the recovery strength is attributed to the re-formation of the strong polymeric network structures in the hydrogels after removing the high shear stress (Ding et al., 2021; Liu et al., 2017). The hydrogel containing both SF and CNPs exhibited greater recovery strength than others due to a higher number of functional groups, which formed more polymeric network structures. These results suggested that the developed hydrogels have good thixotropic property, and can be applied for printing applications.

3.3. Swelling and degradation behavior of the scaffolds

The swelling efficiency of the printed scaffolds was evaluated in water at room temperature to examine the hydrophilicity of the fabricated scaffolds. Hydrophilicity is an important criterion for the assessment of biomaterials for biomedical applications. The hydrophilicity of the scaffolds is also significant for the absorption of body fluids and the transfer of cell nutrients and metabolites. The swelling efficiencies of the developed scaffolds are shown in (Fig. 4a). The composite scaffolds demonstrated a higher swelling efficiency (840 → 3670%) than the pure
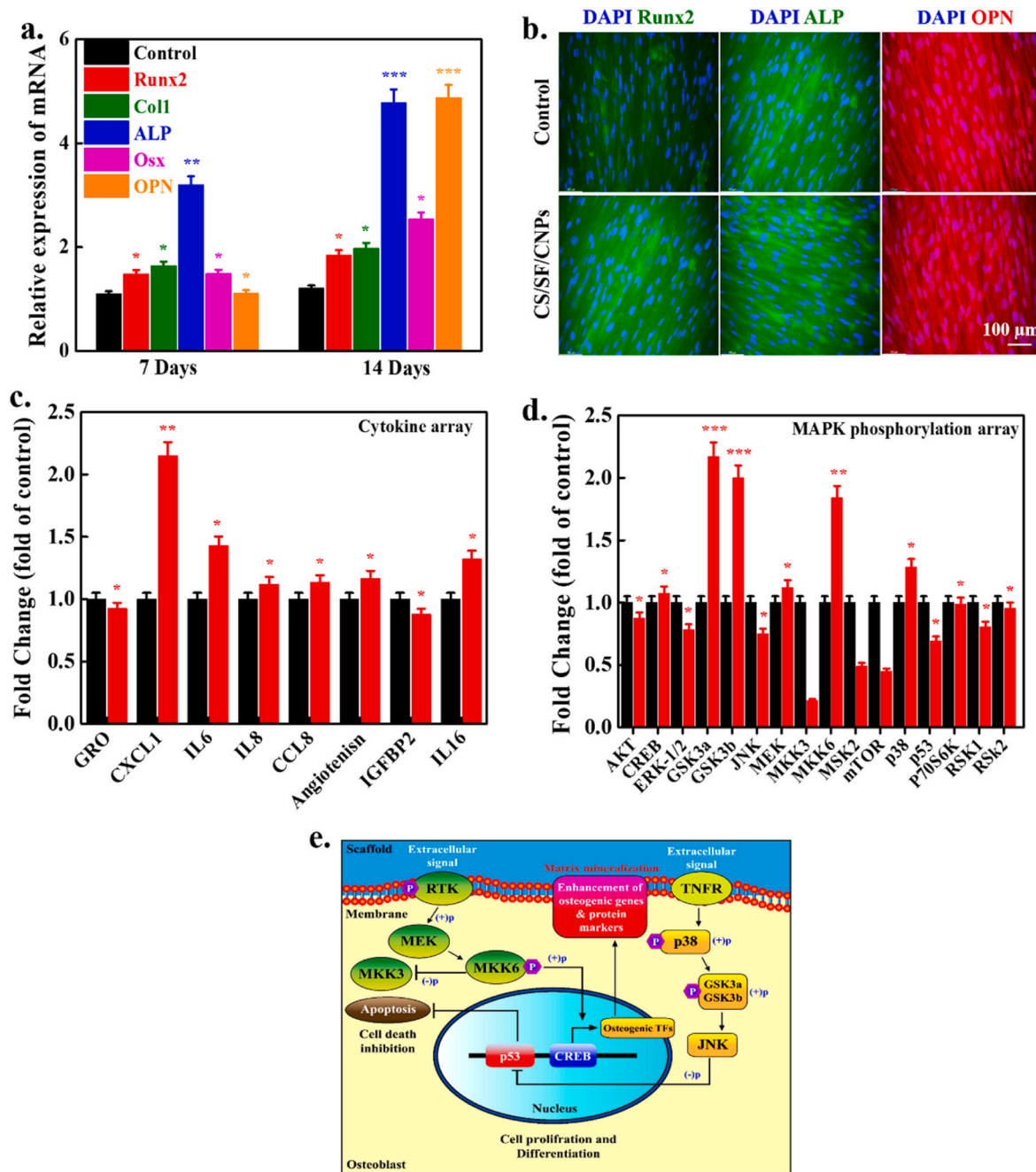
Fig. 6. Evaluation of osteogenic differentiation potential of the fabricated scaffolds, (a) The relative expression of mRNA in hBMSCs with CS/SF/CNPs scaffolds and control after 7 and 14 days of treatment, (b) Expression of osteogenic protein markers in hBMSCs with CS/SF/CNPs scaffolds and control after 7 days of treatment, (c) The fold change in secreted cytokines, (d) The fold change in the pMAPK array, and (e) The proposed model for enhanced osteogenesis of hBMSCs in the presence of CS/SF/CNPs scaffolds. (TNFR-Tumor necrosis factor receptor, JNK-c-Jun N-terminal kinase, GSK3a-Glycogen synthase kinase-2 alpha, CREB-The cAMP-response element binding protein, MEK-Mitogen activated extracellular kinase, MKK-Mitogen activated protein kinase, and RTK-Receptor tyrosin kinase). Statistical analysis was performed between the control and treated groups. Statistical significance was considered at $^{*}p < 0.05$, $^{**}p < 0.01$, and $^{***}p < 0.001$.

polymer scaffolds. All scaffolds showed a rapid swelling potential and reached an equilibrium state within 10 h of immersion. After equilibrium, a slow increase in swelling efficiency was observed in all scaffolds. Different factors, such as crystallinity, porosity, and availability of the functional groups, play important roles in the swelling process of the scaffolds (Felfel, Gideon-Adeniyi, Zakir Hossain, Roberts, & Grant, 2019; Patel, Srivastava, Singh, & Singh, 2018). CS/SF/CNPs scaffolds demonstrated greater swelling efficiency than others due to the availability of more functional groups. The higher availability of functional groups facilitates the absorption of water molecules and consequently

improves the swelling efficiency.

Degradation is a crucial feature of scaffolds as biomaterials in tissue engineering applications. The degradation behavior of the developed scaffolds was analyzed in PBS and protease media, and the results are presented in (Fig. 4b & c). The composite scaffolds showed a greater degradation rate than the pure polymer scaffolds under both conditions, indicating the positive effect of the filler on chitosan degradation. Among these (CS, CS/SF, CS/ CNPs, and CS/SF/ CNPs), CS/SF/ CNPs scaffolds exhibited a higher degradation rate than the others. The higher degradation rate of CS/SF/CNPs scaffolds was probably due to the rough

surface with irregular structures, which facilitated the easy insertion of solvent molecules inside the polymer chains and weakened the network structures, leading to a higher degradation rate. The hydrophilic samples are more prone to absorb the surrounding media and pass throughout their structure (Barbeck et al., 2017; Sultana et al., 2021). Zhang et al. were previously reported the higher degradation rate in carboxymethyl chitosan/cellulose nanocrystals-based scaffolds due to the structural damage through the insertion of the media (Zhang et al., 2019a). However, the degradation rate of the developed scaffolds was faster in the protease medium than in PBS. Thus, it is possible to tune the degradation of chitosan by incorporating a suitable filler or a combination of fillers. The degradation rate of chitosan is profoundly affected by the degree of deacetylation, molecular weight, and media. A decrease in the degradation rate of chitosan was observed by increasing the degree of deacetylation (Croisier & Jérôme, 2013; Kean & Thanou, 2010).

3.4. Biocompatibility of the scaffolds

The cytotoxicity of the developed scaffolds was evaluated in hBMSCs using the WST-1 assay at different periods, and the results are shown in (Fig. 5a). The groups without any scaffolds treatment were used as controls. The composite scaffolds exhibited better cell viability than the pure polymer scaffolds and control scaffolds, indicating their biocompatibility. Cell viability increased with increasing culture time, showing that the developed scaffolds have improved biocompatibility and no adverse effects on hBMSCs. Among these (CS, CS/SF, CS/CNPs, and CS/SF/CNPs), CS/SF/CNPs scaffolds exhibited better cellular activity than others, suggesting the positive effects of both (SF and CNPs) fillers on cell viability. Different factors, such as surface chemistry, roughness, texture, and porosity, play significant roles in cell proliferation, viability, and differentiation (Selvaraj & Fathima, 2017). CS/SF/CNPs scaffolds demonstrated improved hydrophilicity compared to the other scaffolds, as observed in swelling results, which facilitated the physicochemical connections between the scaffold surfaces and cells through ionic forces, resulting in better cell proliferation (Patel et al., 2015). The incorporation of SF and CNPs in the chitosan matrix enhanced the cell affinity due to the weakened positive charge densities of chitosan chains by electrostatic interactions with the negative charges of SF and CNPs. The decrease in charge density between the cell membranes and scaffold surfaces favors cell proliferation. An enhancement in cell proliferation in chitosan/silk fibroin scaffolds resulting from the weakened charge densities due to electrostatic interactions was previously reported (Zhang et al., 2011). Additionally, the biocompatibility of silk fibroin also supports cell attachment, spread, and growth. We further examined the live-dead cell densities of hBMSCs by an inverted fluorescence microscope to prove the biocompatibility of the printed scaffolds after 3 days of treatment, and the results are shown in (Fig. S4). The groups without scaffolds treatment were considered as control. No significant adverse effects were observed in the scaffolds treated groups than the control, showing their biocompatibility. The live-cell densities were higher in the scaffolds treated groups than the control, suggesting their improved cytocompatibility.

The fluorescence morphologies of hBMSCs after 4 days of treatment are shown in (Fig. 5b). The groups without scaffolds were used as controls. The cells were healthy and elongated, indicating the biocompatibility of the printed scaffolds. The cell densities were higher in CS/SF/CNPs treated groups than the others. The cells were interconnected and spread over the scaffolds.

ALP is considered an early cell differentiation marker and plays a vital role in mineralization. The nucleation of inorganic phosphates and calcium ions facilitates the mineralization process, enhancing the phosphate level in the surrounding environment. ALP is a transcription factor that hydrolyzes the phosphate ester to increase phosphate levels in local conditions. ALP triggers the downstream cell differentiation factor to promote osteoblast differentiation (Shalumon, Lai, Chen, & Chen, 2015). ALP activity of hBMSCs cultured on the developed

scaffolds after 7 and 14 days of treatment is shown in (Fig. 5c). The groups without any treatment were used as controls. The composite scaffolds exhibited higher ALP activity than the pure polymer scaffolds and control after 7 days of treatment, indicating their better ALP triggering potential. This potential was further increased after 14 days of composite scaffold treatment, indicating improved ALP activity. Among these (CS, CS/SF, CS/CNPs, and CS/SF/CNPs), CS/SF/CNPs scaffolds exhibited significantly greater ALP activity than the other scaffolds owing to their better cellular activity. The enhanced ALP activity of the CS/SF/CNPs scaffold indicates its osteoconductive nature and could be applied for osteoblasts differentiation.

The mineralization potential of the developed scaffolds was evaluated using the ARS technique in the presence of hBMSCs after 7 and 14 days of treatment, and the results are presented as optical density in (Fig. 5d). Mineralization causes the deposition of calcium phosphate on the surface of the scaffolds. The composite scaffold-treated groups demonstrated higher optical density values than the pure polymer-treated groups and the control after 7 days of treatment, showing its superior mineralization potential. This value further increased after 14 days of treatment, suggesting improved mineralization potential. CS/SF/CNPs scaffolds showed higher mineralization potential than other scaffolds due to their superior cellular activity, facilitating mineralization *via* cell-mediated deposition of ECM constituents. During the differentiation of hBMSCs on the scaffold surface, the anionic matrix of the scaffolds bound the calcium ions first, followed by phosphate ions, leading to calcification *via* nucleation and growth. CS/SF/CNPs scaffolds have plenty of anionic matrices contributed from CNPs and silk fibroin compared to other scaffolds. Therefore, more calcification occurred in the CS/SF/CNPs-treated groups than in the other groups (Kim et al., 2011; Lai, Shalumon, Chen, & Chen, 2014; Wu et al., 2019).

3.5. Osteogenic gene expression and pathway analysis

The osteogenic-associated gene expression in hBMSCs in the presence of the developed scaffolds was evaluated by q-PCR, and the results are shown in (Fig. 6a). The experiment sets without any treatment were used as control. Here, we chose CS/SF/CNPs scaffolds as experimental groups because of their superior cellular activity compared to other scaffolds. The CS/SF/CNPs-treated groups showed higher expression of osteogenic-associated genes (*Runx2, Col1, ALP, Osx,* and *OPN*) than the control after 7 days of treatment, demonstrating its superior osteogenic potential. The expression levels further increased after 14 days of treatment, showing improved osteogenic potential. Bone formation is a complex biological process that involves endochondral and intramembranous ossification. Endochondral ossification is the major process of bone formation and requires cartilage templates. In intramembranous ossification, bone formation occurs directly from mesenchymal condensation. Osteoblast differentiation of mesenchymal stem cells is prominently affected by different transcription factors and signaling proteins (Tang, Li, Osimiri, & Zhang, 2011). Runx2 expression occurs at the early stage of osteogenic differentiation, and differentiation has not occurred without this marker. Runx2 expression was higher in CS/SF/CNPs treated media than in control, demonstrating its osteogenic potential (Kim, Shin, Kim, Kim, & Ryoo, 2020). Col1 is a bone protein found in bone cells. Its expression was also higher in the scaffold-treated media than in control. ALP is an important osteogenic gene marker, and a greater ALP expression indicates the presence of preosteoblasts and osteoblasts at the time of differentiation for bone mineralization (Patel, Dutta, Hexiu, Ganguly, & Lim, 2020). The Osx is an important osteogenic-associated transcription factor that plays a vital role in osteoblast differentiation and bone formation. Osx expression levels were higher in the scaffold-treated groups than in control, indicating osteogenic efficiency. Osx coordinates osteoblast differentiation and proliferation at the time of bone formation OPN is a crucial osteogenic gene marker responsible for cell attachment, apatite formation, and growth (Gupta et al., 2016). OPN expression was higher in CS/SF/
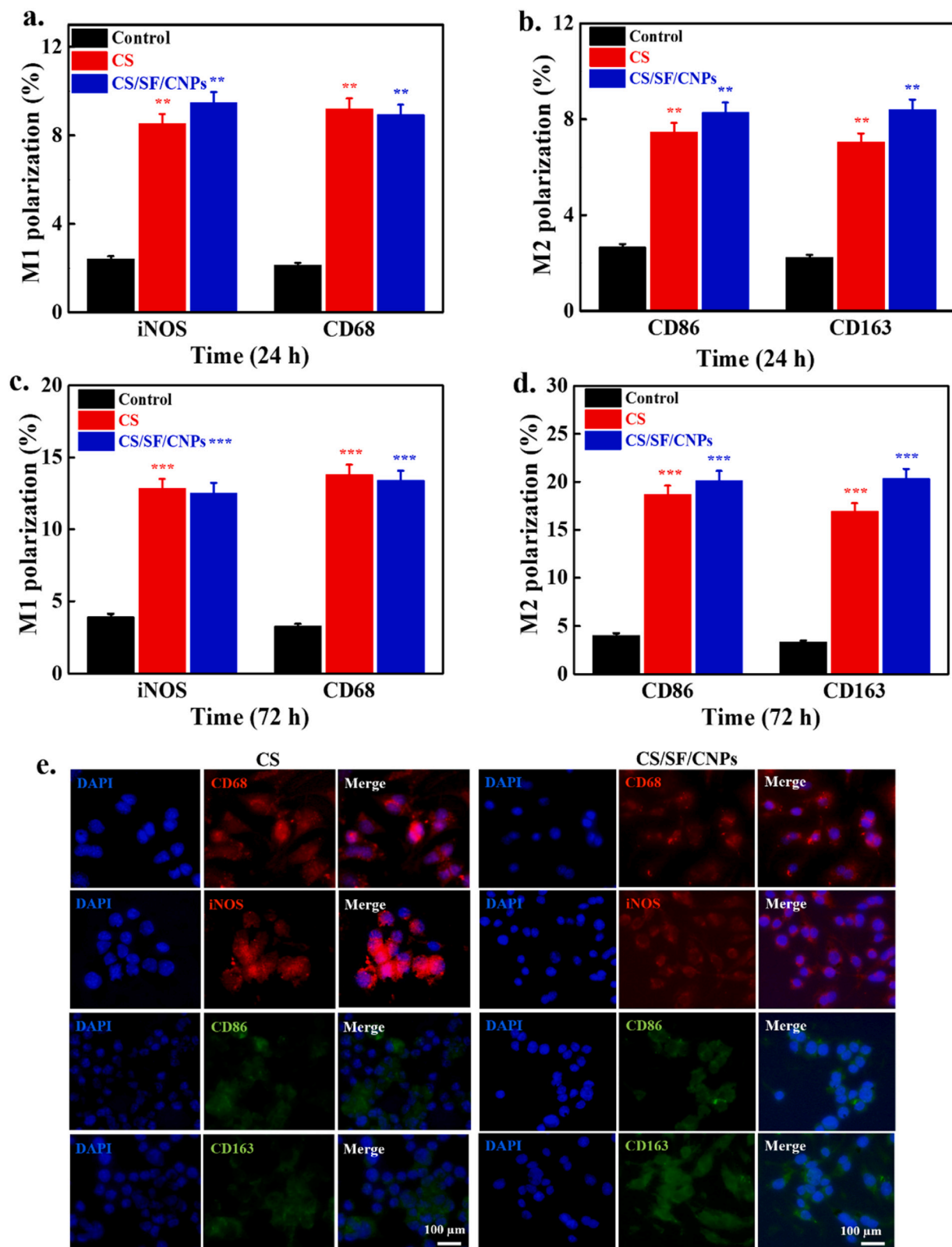
Fig. 7. (a–d) Evaluation of the macrophage polarization potential of the printed scaffolds with Raw 264.7 cells by the FACS technique after 1 and 3 days of treatment, and (e) The immunofluorescence morphologies of the cultured cells to examine the expression of macrophages-associated gene markers (CD68, iNOS, CD86, and CD163). Statistical analysis was performed between the control and treated groups. Statistical significance was considered at $^{**}p < 0.01$, and $^{***}p < 0.001$.

CNPs-treated media than in the control after 14 days of treatment, indicating the superior osteogenic efficiency of the developed scaffolds. The osteogenic differentiation process is significantly affected by the physicochemical properties of the treated materials. It was observed that the materials with hydroxyl functional groups exhibited better osteogenic potential than the other functional groups. The hydroxyl groups facilitate apatite formation in the ECM, leading to rapid bone formation and growth (Li et al., 2015a). The presence of abundant hydroxyl groups in the CS/SF/CNPs scaffolds contributed by CNPs and SF assists higher apatite formation in the ECM, showing better osteogenic potential than the control. Additionally, the favorable surface topography and hydrophilicity of the developed scaffold facilitated improved cellular response, leading to superior osteogenesis (Amiryaghoubi et al., 2020; Kasoju & Bora, 2012; Li et al., 2014).

The expression of different kinds of osteogenic proteins Runx2, ALP, and OPN was also examined by immunofluorescence staining in the presence of CS/SF/CNPs scaffolds after 7 days of treatment, and the results are presented in (Fig. 6b). The groups without any treatment were used as controls. The expression of osteogenic-associated protein markers indicates their osteogenic potential. The expression of osteogenic-associated protein markers was also confirmed by immunohistochemistry (IHC), and the images are shown in (Fig. S5a). Higher expression of osteogenic proteins was observed in the CS/SF/CNPs treated groups than in control, indicating the superior osteogenic potential of the developed scaffolds. The quantitative values of the osteogenic-associated protein markers are shown in (Fig. S5b). The expression levels of Runx2, ALP, and OPN were higher in CS/SF/CNPs treated media than in the control, showing the improved osteogenic ability of the developed scaffolds. The higher expression of osteogenic protein supports superior mineralization and greater osteogenic gene expression potential of the CS/SF/CNPs scaffolds (Mazzoni et al., 2021).

Different pro-and anti-inflammatory cytokines are secreted during events ranging from the host immune response to microbial infections or tissue damage. The secretion of different kinds of cytokines in the presence of the CS/SF/CNPs scaffolds in serum-starved hBMSCs after 24 h of treatment was analyzed using the Raybiotech Human Cytokine Array C1, and the results are presented in (Fig. S6a). The groups receiving no treatment were used as controls. The CS/SF/CNPs treated groups showed a more intense spot than the control group in the cytokine array membrane. The fold change in secreted cytokines is shown in (Fig. 6c). An enhancement in the secretion levels of CXCL1 (2.1), IL6 (1.4), IL8 (1.1), and IL16 (1.3) was observed in the CS/SF/CNPs-treated groups compared to the control, showing its positive effects on cytokine secretion. Interleukin-6 (IL6) is a well-known pro-inflammatory cytokine responsible for signal transduction and recruitment of various chemokines (Tanaka, Narazaki, & Kishimoto, 2014). CXCL1 plays a significant role in the host immune response, for microbial killing at the damage or infection site. CXCL1 recruits and activates neutrophils and binds with glycosaminoglycan (GAG) on epithelial and endothelial cells and the ECM (Girbl et al., 2018; Sawant et al., 2016). The higher secretion of CXCL1 in the presence of CS/SF/CNPs scaffolds indicates its anti-inflammatory potential. The relative expression profiles of different cytokines are shown in (Fig. S6b). The expression levels were higher in CS/SF/CNPs-treated groups than in the controls.

The signaling mechanism of the scaffold-mediated improved osteogenesis of hBMSCs was monitored by a MAPK phosphorylation array (pMAPK array), and the results are shown in (Fig. S7a). The groups without any treatment were considered as the controls. The scaffold-treated groups exhibited a more intense spot in the membrane than the control group. The fold change in the pMAPK array is shown in (Fig. 6d). The p38, MKK3, GSK3b, and GSK3a levels were upregulated by 1.28-, 1.84-, 2.0-, and 2.1-fold, respectively. Osteogenic differentiation is profoundly affected and regulated by extracellular kinases, such as ERK or MAPK. Phosphorylation of the kinase domain of these receptors activates a series of the signal cascade, leading to the activation or inhibition of specific transcription factors (Wang, Lin, Chang, & Sun,

2013). In the present study, the higher expression of these phosphorylated kinases in the presence of the CS/SF/CNPs scaffolds stimulated the osteogenic differentiation and promoted the secretion of inflammatory cytokines. Enhanced osteogenic differentiation of stem cells *via* these phosphorylated kinases was previously reported (Liu, Miao, Shi, Gao, & Wang, 2020). The relative expression profiles of different MAPK phosphorylation arrays are given in (Fig. S7b). The expression levels were higher in CS/SF/CNPs-treated groups compared to the controls. Based on these results, we propose a mechanistic approach for enhanced cell proliferation and differentiation of hBMSCs in the presence of CS/SF/CNPs scaffolds. The model is presented in (Fig. 6e).

3.6. Macrophage polarization study

Cytotoxicity is the essential criterion of the implanted biomaterials for tissue engineering. The cytotoxicity of the printed scaffolds was also examined with Raw 264.7 cells after different periods, and the results are shown in (Fig. S8). The groups without the scaffolds treatment were considered to be the control. The groups having printed scaffolds exhibited greater cell viability than control, suggesting their accelerating effects on cell proliferation. Among these (CS, CS/SF, CS/CNPs, and CS/SF/CNPs), CS/SF/CNPs scaffolds showed higher cell viability than other scaffolds, indicating best cytocompatibility (Zhong et al., 2021). Macrophages are immune cells and play significant roles in the physiological response to the implanted materials. It has been observed that the classically polarized M1 macrophages facilitated angiogenesis in the early stage of implantation, which assisted the vascularization in the newly generated tissue. However, prolonged activation of M1 macrophages around the implanted area causes the pro-inflammation *via* interferon-gamma (IFN-γ) or lipopolysaccharide (LPS) (Li et al., 2018). The M2 phenotype macrophage polarization favors bone regeneration by triggering the secretion of different cytokines and growth factors, including vascular endothelial growth factor (VEGF) and bone morphogenetic protein 2 (BMP2). To examine the macrophage polarization potential of the printed scaffolds (CS and CS/SF/CNPs), we performed the FACS experiment to measure the percentage expression values for M1 and M2 macrophages with the printed scaffolds, and the expressed values are shown in (Fig. 7a–d). Here, we considered the iNOS, CD68 as M1 polarization markers, and CD163 as M2 polarization markers (Chen et al., 2020). CD86 is considered an M2b macrophage marker. However, several studies revealed it to identify M1 macrophages (Wang, Zhang, Wu, Rong, & Guo, 2018). The groups without scaffolds treatment were taken control. Initially, the value of M1 polarization was slightly higher than M2 after 1 day of treatment, suggesting the pro-inflammatory effects of the Raw 264.7 cells in the presence of the scaffolds (Brown, Valentin, Stewart-Akers, McCabe, & Badylak, 2009). However, an enhancement in M2 macrophage polarization occurred in the printed scaffolds after 3 days of incubation, indicating the modulatory potential of the printed scaffolds. This enhancement was higher in CS/SF/CNPs than CS scaffolds and control. The phenotypic transformation from M1 to M2 is favorable for improved bone regeneration (Xiang et al., 2020). These results suggested that the 3D-printed scaffolds have macrophage modulation potential (M1 → M2), and can be an attractive platform for macrophage modulatory or healing functions. The FACS results of Raw 264.7 cells treated with the printed scaffolds are given in (Fig. S9). A Similar expression of both can be observed in the FACS results.

We further examined the fluorescence expression of macrophage-associated gene markers (iNOS, CD68, CD86, and CD163) after 3 days of treatment, and the results are presented in (Fig. 7e). Here, we have chosen the CS and CS/SF/CNPs for the experiment to observe the change in intensity/morphologies of the cultured Raw 264.7 cells after 3 days due to the improved expression of macrophage phenotypes than control. The immunofluorescence staining indicated the greater intensity/expression of M2b/M2 phenotype CD86, and CD163 markers occurred in CS/SF/CNPs scaffolds treated groups than CS scaffolds, showing M2
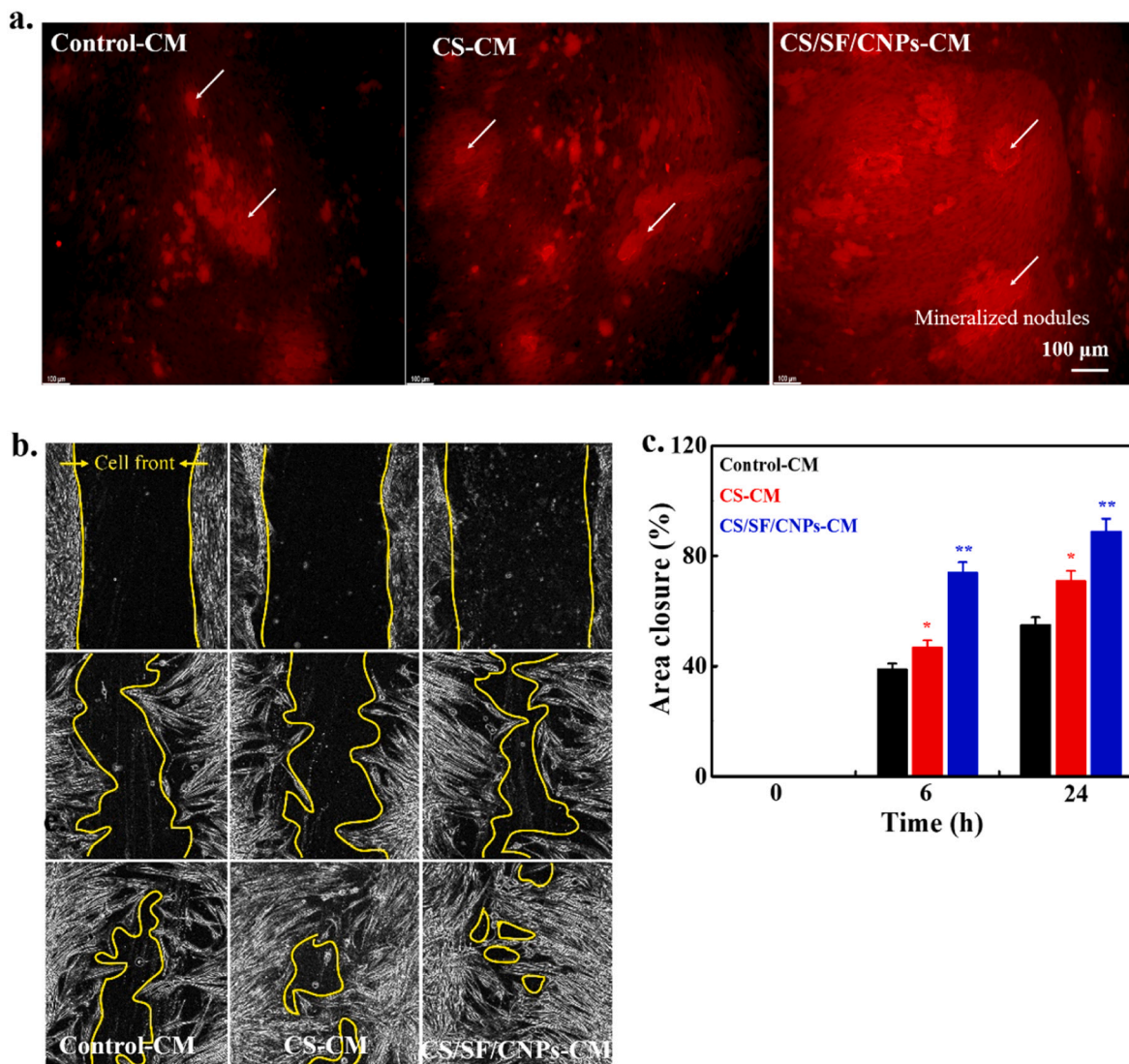
Fig. 8. (a) Evaluation of the osteo-immunomodulatory potential of the printed scaffolds with hBMSCs in the presence of macrophages-derived conditioned media (M-CM) (arrows indicate the formed mineralized nodules), (b) Migration ability of hBMSCs with the printed scaffolds in M-CM, and (c) Quantification of the closed area with the printed scaffolds in M-CM at indicated periods. Statistical analysis was performed between the control and treated groups. Statistical significance was considered at $^*p < 0.05$, and $^{**}p < 0.01$.

phenotype polarization potential of the scaffolds. The morphological change was also observed in CD86, and CD163 expressed cells, while cells with iNOS, and CD68 markers exhibited nearly spherical morphology. This is attributed to the formation of the multinucleated giant cells in the presence of the scaffolds, which further differentiate into M2 macrophage phenotype (Kazimierczak, Koziol, & Przekora, 2021). The above results indicated that the scaffolds facilitate M2 macrophage differentiation *in vitro*, triggering the secretion of different growth factors and proteins, facilitating improved bone regeneration *via* the macrophage-mediated process.

3.7. Macrophage mediated osteogenesis and migration study

The osteo-immunomodulatory effects of the implanted biomaterials significantly influence bone regeneration. The biomaterials that exhibited greater M2 polarization potential are closely related to osteogenesis and promoted bone regeneration (Ariganello, Simionescu, Labow, & Michael Lee, 2011). In order to evaluate the osteo-immunomodulatory potential of 3D-printed scaffolds, we examined the mineralization potential of hBMSCs with scaffolds in the presence of

M-CM by the ARS staining method after 7 days of treatment *in vitro*, and the results are shown in (Fig. 8a). Here, we chose CS and CS/SF/CNPs scaffolds for this experiment. The groups without treatment were taken as control. The scaffolds treated groups exhibited intense red color than the control, due to the greater deposition of the mineralized nodules. The CS/SF/CNPs treated groups demonstrated more intense color than CS scaffolds improving mineralization efficiency. The apatite formation is an essential process in osteogenesis (Boonrungsiman et al., 2012). The greater apatite formation occurred with the scaffolds in the presence of M-CM, suggesting the osteo-immunomodulation potential of the scaffolds, which have significant roles in bone tissue regeneration (Tan et al., 2020).

The migration ability of hBMSCs was also analyzed in the M-CM after 6 and 24 h of treatment, and the results are presented in (Fig. 8b). The groups without scaffolds treatment were taken as control. The cell migration densities were high in the scaffolds treated groups than the control after 6 h of incubation, showing the positive effects of the biomaterial in cell migration. The cell densities were further increased in the scaffolds treated media after 24 h of incubation, indicating improved migration potential. This was more significant with CS/SF/CNPs
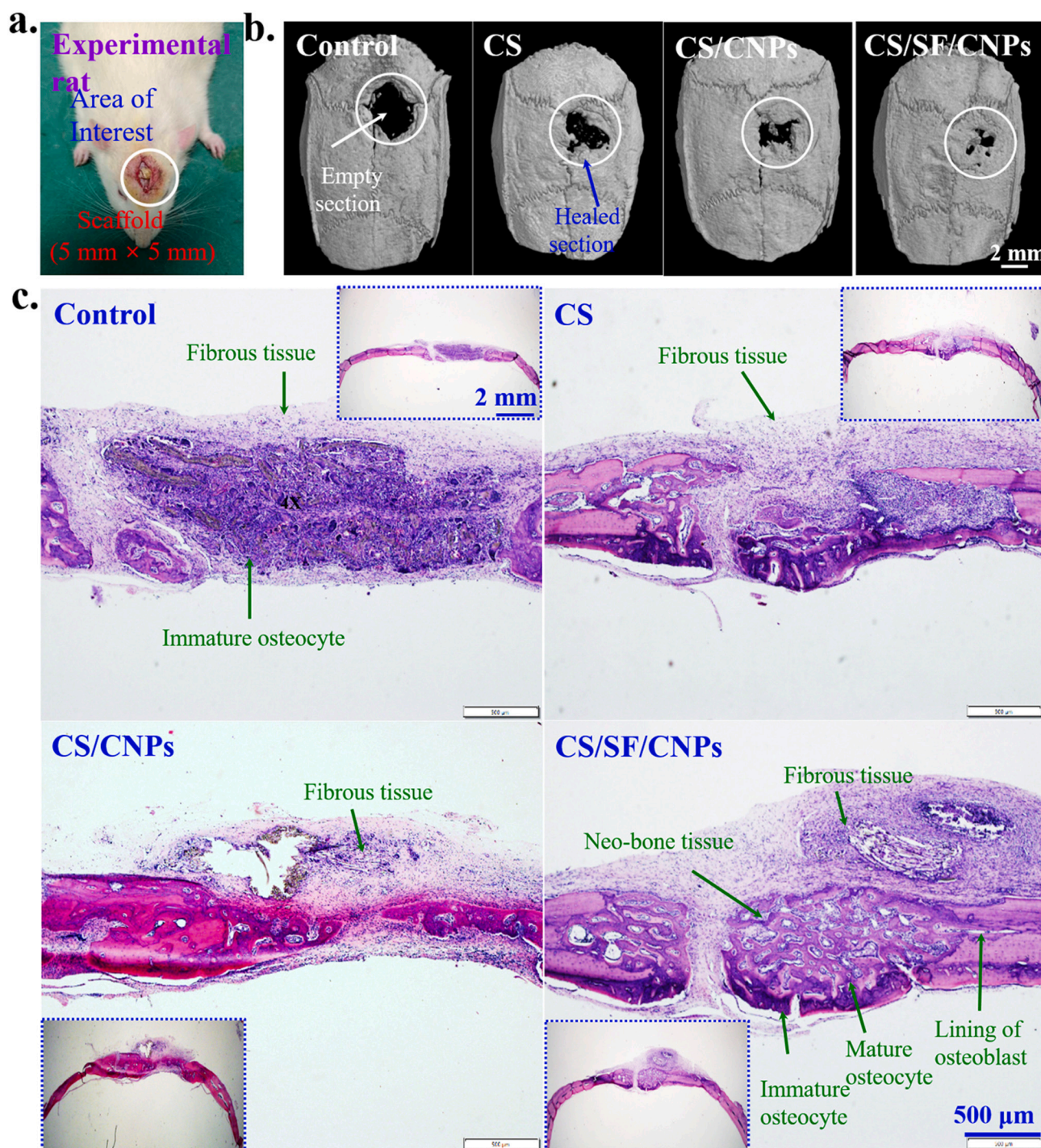
Fig. 9. *In vivo* study for the evaluation of the osteogenic potential of the printed scaffold, (a) The obtained CT images in different conditions. The circle shows the defective area in the rats. White and blue arrows indicate the empty and healed section of the rat after 5 weeks of implantation, and (b) H&E stained images of the newly generated bone tissues after 5 weeks of implantation in different conditions. (Inset images are in low resolution). (For interpretation of the references to color in this figure legend, the reader is referred to the web version of this article.)

scaffolds compared to the other. The greater migration ability of hBMSCs in CS/SF/CNPs scaffolds is attributed to its better cellular activity. This potential is highly required in wound healing applications. We also measured the migrant cells in terms of wound closure, and the results are shown in (Fig. 8c). The percentage of area closure was high with scaffold groups' vis-à-vis control after 6 h of incubation, and this was more prominent in CS/SF/CNPs scaffolds, which further increased after 24 h of treatment, demonstrating its better wound healing potential. In other words, the printed scaffold expressively promotes wound healing *in vitro*.

3.8. In vivo bone regeneration potential and histological analysis

The *in vivo* bone regeneration potential of the printed scaffold was assessed in the rat calvarial defect model after 5 weeks of implantation, and the results are presented in (Fig. 9). A photograph of a defective rat with the implanted scaffold is given in (Fig. 9a). The healing of the defective area was monitored by computed tomography (CT), and the

Table 1
The quantitative values for the newly generated bone tissues in the rats in different conditions after 5 weeks of implantation.

Sample	Bone volume (BV) (mm³)	Bone volume fraction (BV/TV) (%)	Trabecular number (Tb·N) (1/mm)	Trabecular thickness (Tb·Th) (mm)	Trabecular separation (Tb·Sp) (mm)	Bone mineral density (BMD) (g/cm³)
Control	2.03396 ± 0.101	3.1624 ± 0.158	0.09374 ± 0.004	0.33736 ± 0.016	1.84006 ± 0.09	0.11971 ± 0.005
CS	5.39574 ± 0.2697	8.38928 ± 0.419	0.20485 ± 0.01	0.40954 ± 0.020	1.32593 ± 0.065	0.15731 ± 0.007
CS/CNPs	9.53612 ± 0.4760	14.82675 ± 0.700	0.26676 ± 0.013	0.5558 ± 0.025	1.27297 ± 0.060	0.22809 ± 0.010
CS/SF/CNPs	13.11016 ± 0.610	20.38366 ± 1.01	0.36996 ± 0.017	0.55096 ± 0.025	1.14538 ± 0.055	0.31173 ± 0.015

obtained images are shown in (Fig. 9b). The CS/SF/CNPs-treated scaffolds exhibited a greater healing potential than the positive (CS scaffolds) and negative groups (without treatment) after 5 weeks of implantation, showing their improved bone regeneration potential. Moreover, no implantation was noted near the implanted sites, indicating the superior biocompatibility of the developed scaffold (Patel et al., 2020). Bone volume (BV), bone volume fraction (BV/TV), trabecular number (Tb.N), trabecular thickness (Tb.Th), trabecular separation (Tb.Sp), and bone mineral density (BMD) are shown in Table 1. The BV, BV/TV, Tb.N, Tb.Th, and BMD values were significantly higher in CS/SF/CNPs scaffold-treated rats than in the other groups, indicating that the CS/SF/CNPs scaffold significantly promoted bone regeneration (Wang et al., 2019), and the Tb.Sp value was lower in CS/SF/CNPs treated rats than in other groups, demonstrating the compact arrangement of the newly developed bone tissue.

CT results indicated that bone formation occurred from the periphery of the defected bones towards the inside of the grafted scaffolds. The superior biocompatibility and osteogenic potential of the CS/SF/CNPs scaffolds triggered the regeneration of new tissues *via* cell-matrix interaction (Zhou et al., 2013). Different growth factors, such as bone morphogenetic proteins (BMPs), transforming growth factor (TGF-β), insulin-like growth factor (IGF), vascular endothelial growth factor (VEGF), and platelet-derived growth factor (PDGF) play important roles in cell behavior during tissue regeneration. Cells from the bone microenvironment, including inflammatory cells, and fibroblasts secrete their growth factors (Zhang et al., 2019c). The upregulation of TGF-β was earlier reported in fibroin/CNPs-based scaffolds, which stimulated the regeneration of new bone tissues (Chen, Zhou, Chen, & Chen, 2016). Therefore, it is anticipated that promoting different kinds of osteogenic-associated genes and stimulating different growth factors might be crucial reasons for the enhanced bone regeneration potential of CS/SF/CNPs scaffolds compared to that of the others *via* the MAPK phosphorylation pathway.

Hematoxylin and Eosin (H&E) analysis was performed to examine the newly generated bone tissues in the rats after 5 weeks of implantation, and the results are shown in (Fig. 9c). The generation of new bone tissue was observed in all groups, and no inflammatory cells were detected near the implanted sites. However, the density of newly generated cells was higher in CS/SF/CNPs-treated rats than in the other groups. This finding is well supported by our CT results (Fig. 9b), where improved bone healing was observed. The CS/SF/CNPs-treated rats showed more mature osteocyte cells, indicating improved bone-promoting effects. The H&E staining results demonstrate that the developed scaffolds have greater osteogenic efficiency and can be applied as an attractive biomaterial for rapid bone regeneration.

4. Conclusions

Composite scaffolds of chitosan were printed using SF and CNPs as reinforcing agents for bone tissue regeneration. Composite scaffolds containing SF and CNPs in the polymer matrix showed superior rheological and swelling potential compared than pure polymer hydrogel scaffolds or individually incorporated scaffolds. The composite hydrogels exhibited better recovery strength than the pure polymer hydrogel. An enhanced degradation rate was observed in CS/SF/CNPs scaffolds

compared to other scaffolds, demonstrating the positive effects of SF and CNPs. The improved cellular activity was observed in the CS/SF/CNPs scaffold-treated groups compared to other groups, indicating superior biocompatibility and bioactivity of the scaffolds. Higher mineralization was observed in the composite treated groups compared to the control and pure polymer scaffolds, and which was more significant in CS/SF/CNPs scaffold-treated media. Enhanced osteogenic-associated genes and protein expression occurred in the CS/SF/CNPs scaffold-treated groups compared to the control, indicating its superior osteogenic potential. The protein array indicates that the osteogenic induction process predominantly occurs *via* the mitogen-activated protein kinase (MAPK) pathway. Increased secretion of CXCL1 chemokine occurred in CS/SF/CNPs scaffold-treated media compared to the control, showing its neutrophil activation potential for immune response. The printed scaffolds activated the M2 phenotype macrophages polarization and osteoimmunomodulation, which aided bone tissue regeneration. Improved bone regeneration was observed in CS/SF/CNPs-treated rats compared to those in the control group, showing its superior bone healing potential.

Furthermore, H&E-stained images indicated that the CS/SF/CNPs-treated rats had higher densities of mature osteocytes than the other treated groups. Based on these findings, we concluded that the printed scaffolds have bioactive, biodegradable, and osteoconductive potential and can be used as an attractive biomaterial for bone tissue engineering.

Data availability

The data used to support the findings of this study are available from the corresponding author upon request.

CRediT authorship contribution statement

Dinesh K. Patel: Conceptualization, fabrication, characterizations, and writing the manuscript. **Sayan Deb Dutta and Keya Ganguly**: Cytotoxicity, ALP assay and immunohistochemistry experiments. **Jin Hexiu**: Performed the surgeries, collected micro CT and H&E images. **Ki-Taek Lim**: Supervision, funding acquisition, project administration, writing-review and editing.

Declaration of competing interest

The authors declare that they have no known competing financial interests or personal relationships that could have appeared to influence the work reported in this paper.

Appendix A. Supplementary data

Supplementary data to this article can be found online at https://doi.

org/10.1016/j.carbpol.2021.119077.

References

Abouzeid, R. E., Khiari, R., Beneventi, D., & Dufresne, A. (2018). Biomimetic mineralization of three-dimensional printed Alginate/TEMPO-oxidized cellulose nanofibril scaffolds for bone tissue engineering. *Biomacromolecules, 19*, 4442–4452.

Ambre, A. H., Katti, K. S., & Katti, D. R. (2010). Nanoclay based composite scaffolds for bone tissue engineering applications. *Journal of Nanotechnology in Engineering and Medicine, 1*, 031013-031023.

Amir Afshar, H., & Ghaee, A. (2016). Preparation of aminated chitosan/alginate scaffold containing halloysite nanotubes with improved cell attachment. *Carbohydrate Polymers, 151*, 1120–1131.

Amiryaghoubi, N., Fathi, M., Pesyan, N. N., Samiei, M., Barar, J., & Omidi, Y. (2020). Bioactive polymeric scaffolds for osteogenic repair and bone regenerative medicine. *Medicinal Research Reviews, 40*, 1833–1870.

Ariganello, M. B., Simionescu, D. T., Labow, R. S., & Michael Lee, J. (2011). Macrophage differentiation and polarization on a decellularized pericardial biomaterial. *Biomaterials, 32*, 439–449.

Asadi-Eydivand, M., Solati-Hashjin, M., Farzad, A., & Abu Osman, N. A. (2016). Effect of technical parameters on porous structure and strength of 3D printed calcium sulfate prototypes. *Robotics and Computer-Integrated Manufacturing, 37*, 57–67.

Baek, D., Park, K. H., Lee, K.-M., Jung, S., Joung, S., Kim, J., & Lee, J. W. (2021). Ubiquitin-specific protease 53 promotes osteogenic differentiation of human bone marrow-derived mesenchymal stem cells. *Cell Death & Disease, 12*, 238–253.

Barbeck, M., Serra, T., Booms, P., Stojanovic, S., Najman, S., Engel, E., Sader, R., Kirkpatrick, C. J., Navarro, M., & Ghanaati, S. (2017). Analysis of the in vitro degradation and the in vivo tissue response to bi-layered 3D-printed scaffolds combining PLA and biphasic PLA/bioglass components – guidance of the inflammatory response as basis for osteochondral regeneration. *Bioactive Materials, 2*, 208–223.

Boonrungsiman, S., Gentleman, E., Carzaniga, R., Evans, N. D., McComb, D. W., Porter, A. E., & Stevens, M. M. (2012). The role of intracellular calcium phosphate in osteoblast-mediated bone apatite formation. *Proceedings of the National Academy of Sciences, 109*, 14170–14175.

Brown, B. N., Valentin, J. E., Stewart-Akers, A. M., McCabe, G. P., & Badylak, S. F. (2009). Macrophage phenotype and remodeling outcomes in response to biologic scaffolds with and without a cellular component. *Biomaterials, 30*, 1482–1491.

Chen, M., Zhang, Y., Zhou, P., Liu, X., Zhao, H., Zhou, X., Gu, Q., Li, B., Zhu, X., & Shi, Q. (2020). Substrate stiffness modulates bone marrow-derived macrophage polarization through NF-κB signaling pathway. *Bioactive Materials, 5*, 880–890.

Chen, X., Zhou, R., Chen, B., & Chen, J. (2016). Nanohydroxyapatite/cellulose nanocrystals/silk fibroin ternary scaffolds for rat calvarial defect regeneration. *RSC Advances, 6*, 35684–35691.

Croisier, F., & Jérôme, C. (2013). Chitosan-based biomaterials for tissue engineering. *European Polymer Journal, 49*, 780–792.

Derakhshanfar, S., Mbeleck, R., Xu, K., Zhang, X., Zhong, W., & Xing, M. (2018). 3D bioprinting for biomedical devices and tissue engineering: A review of recent trends and advances. *Bioactive Materials, 3*, 144–156.

Ding, H., Liang, X., Xu, J., Tang, Z., Li, Z., Liang, R., & Sun, G. (2021). Hydrolyzed hydrogels with super stretchability, high strength, and fast self-recovery for flexible sensors. *ACS Applied Materials & Interfaces, 13*, 22774–22784.

Dorishetty, P., Balu, R., Athukoralalage, S. S., Greaves, T. L., Mata, J., de Campo, L., Saha, N., Zannettino, A. C. W., Dutta, N. K., & Choudhury, N. R. (2020). Tunable biomimetic hydrogels from silk fibroin and nanocellulose. *ACS Sustainable Chemistry & Engineering, 8*, 2375–2389.

Dutta, S., Patel, D., Jin, B., Choi, S.-I., Lee, O., & Lim, K.-T. (2021). Effects of cirsium setidens (Dunn) nakai on the osteogenic differentiation of stem cells. *Molecular Medicine Reports, 23*, 264–275.

Eming, S. A., Hammerschmidt, M., Krieg, T., & Roers, A. (2009). Interrelation of immunity and tissue repair or regeneration. *Seminars in Cell & Developmental Biology, 20*, 517–527.

Felfel, R. M., Gideon-Adeniyi, M. J., Zakir Hossain, K. M., Roberts, G. A. F., & Grant, D. M. (2019). Structural, mechanical and swelling characteristics of 3D scaffolds from chitosan-agarose blends. *Carbohydrate Polymers, 204*, 59–67.

Ferreira, F. V., Souza, L. P., Martins, T. M. M., Lopes, J. H., Mattos, B. D., Mariano, M., Pinheiro, I. F., Valverde, T. M., Livi, S., Camilli, J. A., et al. (2019). Nanocellulose/bioactive glass cryogels as scaffolds for bone regeneration. *Nanoscale, 11*, 19842–19849.

Franz, S., Rammelt, S., Scharnweber, D., & Simon, J. C. (2011). Immune responses to implants – A review of the implications for the design of immunomodulatory biomaterials. *Biomaterials, 32*, 6692–6709.

Gao, T., Gillispie, G. J., Copus, J. S., Pr, A. K., Seol, Y.-J., Atala, A., Yoo, J. J., & Lee, S. J. (2018). Optimization of gelatin–alginate composite bioink printability using rheological parameters: A systematic approach. *Biofabrication, 10*, Article 034106.

Girbl, T., Lenn, T., Perez, L., Rolas, L., Barkaway, A., Thiriot, A., del Fresno, C., Lynam, E., Hub, E., Thelen, M., et al. (2018). Distinct compartmentalization of the chemokines CXCL1 and CXCL2 and the atypical receptor ACKR1 determine discrete stages of neutrophil diapedesis. *Immunity, 49*, 1062–1076. e1066.

Gupta, P., Adhikary, M., M, J. C., Kumar, M., Bhardwaj, N., & Mandal, B. B. (2016). Biomimetic, osteoconductive non-mulberry silk fiber reinforced tricomposite scaffolds for bone tissue engineering. *ACS Applied Materials & Interfaces, 8*, 30797–30810.

Hadisi, Z., Nourmohammadi, J., & Mohammadi, J. (2015). Composite of porous starch-silk fibroin nanofiber-calcium phosphate for bone regeneration. *Ceramics International, 41*, 10745–10754.

He, Y., Yang, F., Zhao, H., Gao, Q., Xia, B., & Fu, J. (2016). Research on the printability of hydrogels in 3D bioprinting. *Scientific Reports, 6*, 29977–29990.

Ingole, V. H., Vuherer, T., Maver, U., Vinchurkar, A., Ghule, A. V., & Kokol, V. (2019). Mechanical properties and cytotoxicity of differently structured nanocellulose-hydroxyapatite based composites for bone regeneration application. *Nanomaterials, 10*, 25.

Jin, J., Hassanzadeh, P., Perotto, G., Sun, W., Brenckle, M. A., Kaplan, D., Omenetto, F. G., & Rolandi, M. (2013). A biomimetic composite from solution self-assembly of chitin nanofibers in a silk fibroin matrix. *Advanced Materials, 25*, 4482–4487.

Kasoju, N., & Bora, U. (2012). Silk fibroin in tissue engineering. *Advanced Healthcare Materials, 1*, 393–412.

Kazimierczak, P., Koziol, M., & Przekora, A. (2021). The chitosan/agarose/NanoHA bone scaffold-induced M2 macrophage polarization and its effect on osteogenic differentiation in vitro. *International Journal of Molecular Sciences, 22*, 1109.

Kean, T., & Thanou, M. (2010). Biodegradation, biodistribution and toxicity of chitosan. *Advanced Drug Delivery Reviews, 62*, 3–11.

Kim, G. H., Ahn, S. H., Lee, H. J., Lee, S., Cho, Y., & Chun, W. (2011). A new hybrid scaffold using rapid prototyping and electrohydrodynamic direct writing for bone tissue regeneration. *Journal of Materials Chemistry, 21*, 19138.

Kim, W.-J., Shin, H.-L., Kim, B.-S., Kim, H.-J., & Ryoo, H.-M. (2020). RUNX2-modifying enzymes: Therapeutic targets for bone diseases. *Experimental & Molecular Medicine, 52*, 1178–1184.

Kurian, M., Stevens, R., & McGrath, K. (2019). Towards the development of artificial bone grafts: Combining synthetic biomineralisation with 3D printing. *Journal of Functional Biomaterials, 10*, 12.

Lai, G.-J., Shalumon, K. T., Chen, S.-H., & Chen, J.-P. (2014). Composite chitosan/silk fibroin nanofibers for modulation of osteogenic differentiation and proliferation of human mesenchymal stem cells. *Carbohydrate Polymers, 111*, 288–297.

Lee, K.-Y., Aitomäki, Y., Berglund, L. A., Oksman, K., & Bismarck, A. (2014). On the use of nanocellulose as reinforcement in polymer matrix composites. *Composites Science and Technology, 105*, 15–27.

Li, J., Baker, B. A., Mou, X., Ren, N., Qiu, J., Boughton, R. I., & Liu, H. (2014). Biopolymer/calcium phosphate scaffolds for bone tissue engineering. *Advanced Healthcare Materials, 3*, 469–484.

Li, J. E. J., Kawazoe, N., & Chen, G. (2015a). Gold nanoparticles with different charge and moiety induce differential cell response on mesenchymal stem cell osteogenesis. *Biomaterials, 54*, 226–236.

Li, M., Gao, L., Chen, J., Zhang, Y., Wang, J., Lu, X., Duan, K., Weng, J., & Feng, B. (2018). Controllable release of interleukin-4 in double-layer sol–gel coatings on TiO2 nanotubes for modulating macrophage polarization. *Biomedical Materials, 13*, Article 045008.

Li, Q., Wang, X., Lou, X., Yuan, H., Tu, H., Li, B., & Zhang, Y. (2015b). Genipin-crosslinked electrospun chitosan nanofibers: Determination of crosslinking conditions and evaluation of cytocompatibility. *Carbohydrate Polymers, 130*, 166–174.

Liu, J., Tan, C. S. Y., Yu, Z., Lan, Y., Abell, C., & Scherman, O. A. (2017). Biomimetic supramolecular polymer networks exhibiting both toughness and self-recovery. *Advanced Materials, 29*, Article 1604951.

Liu, L., Miao, Y., Shi, X., Gao, H., & Wang, Y. (2020). Phosphorylated chitosan hydrogels inducing osteogenic differentiation of osteoblasts via JNK and p38 signaling pathways. *ACS Biomaterials Science & Engineering, 6*, 1500–1509.

Liu, M., Zhang, Y., Wu, C., Xiong, S., & Zhou, C. (2012). Chitosan/halloysite nanotubes bionanocomposites: Structure, mechanical properties and biocompatibility. *International Journal of Biological Macromolecules, 51*, 566–575.

Liu, Q., Li, Q., Xu, S., Zheng, Q., & Cao, X. (2018). Preparation and properties of 3D printed alginate-chitosan polyion complex hydrogels for tissue engineering. *Polymers, 10*, 664.

Mazzoni, E., Mazziotta, C., Iaquinta, M. R., Lanzillotti, C., Fortini, F., D'Agostino, A., Trevisiol, L., Nocini, R., Barbanti-Brodano, G., Mescola, A., et al. (2021). Enhanced osteogenic differentiation of human bone marrow-derived mesenchymal stem cells by a hybrid hydroxylapatite/collagen scaffold. *Frontiers in Cell and Developmental Biology, 8*, 610570–610578.

Mitra, J., Tripathi, G., Sharma, A., & Basu, B. (2013). Scaffolds for bone tissue engineering: Role of surface patterning on osteoblast response. *RSC Advances, 3*, 11073.

Osathanon, T., Linnes, M. L., Rajachar, R. M., Ratner, B. D., Somerman, M. J., & Giachelli, C. M. (2008). Microporous nanofibrous fibrin-based scaffolds for bone tissue engineering. *Biomaterials, 29*, 4091–4099.

Patel, D. K., Dutta, S. D., Ganguly, K., Kim, J. W., & Lim, K. T. (2021a). Enhanced osteogenic potential of unzipped carbon nanotubes for tissue engineering. *Journal of Biomedical Materials Research Part A, 109*, 1869–1880.

Patel, D. K., Dutta, S. D., Ganguly, K., & Lim, K.-T. (2021b). Multifunctional bioactive chitosan/cellulose nanocrystal scaffolds eradicate bacterial growth and sustain drug delivery. *International Journal of Biological Macromolecules, 170*, 178–188.

Patel, D. K., Dutta, S. D., Hexiu, J., Ganguly, K., & Lim, K.-T. (2020). Bioactive electrospun nanocomposite scaffolds of poly(lactic acid)/cellulose nanocrystals for bone tissue engineering. *International Journal of Biological Macromolecules, 162*, 1429–1441.

Patel, D. K., Dutta, S. D., & Lim, K.-T. (2019). Nanocellulose-based polymer hybrids and their emerging applications in biomedical engineering and water purification. *RSC Advances, 9*, 19143–19162.

Patel, D. K., Dutta, S. D., Shin, W.-C., Ganguly, K., & Lim, K.-T. (2021c). Fabrication and characterization of 3D printable nanocellulose-based hydrogels for tissue engineering. *RSC Advances, 11*, 7466–7478.

Patel, D. K., Rana, D., Aswal, V. K., Srivastava, S., Roy, P., & Maiti, P. (2015). Influence of graphene on self-assembly of polyurethane and evaluation of its biomedical properties. *Polymer, 65*, 183–192.

Patel, S., Srivastava, S., Singh, M. R., & Singh, D. (2018). Preparation and optimization of chitosan-gelatin films for sustained delivery of lupeol for wound healing. *International Journal of Biological Macromolecules, 107*, 1888–1897.

Pati, F., Jang, J., Ha, D.-H., Won Kim, S., Rhie, J.-W., Shim, J.-H., Kim, D.-H., & Cho, D.-W. (2014). Printing three-dimensional tissue analogues with decellularized extracellular matrix bioink. *Nature Communications, 5*, 3935–3946.

Rashad, A., Mohamed-Ahmed, S., Ojansivu, M., Berstad, K., Yassin, M. A., Kivijärvi, T., Heggset, E. B., Syverud, K., & Mustafa, K. (2018). Coating 3D printed polycaprolactone scaffolds with nanocellulose promotes growth and differentiation of mesenchymal stem cells. *Biomacromolecules, 19*, 4307–4319.

Sawant, K. V., Poluri, K. M., Dutta, A. K., Sepuru, K. M., Troshkina, A., Garofalo, R. P., & Rajarathnam, K. (2016). Chemokine CXCL1 mediated neutrophil recruitment: Role of glycosaminoglycan interactions. *Scientific Reports, 6*, 33123–331301.

Selvaraj, S., & Fathima, N. N. (2017). Fenugreek incorporated silk fibroin nanofibers—A potential antioxidant scaffold for enhanced wound healing. *ACS Applied Materials & Interfaces, 9*, 5916–5926.

Shalumon, K. T., Lai, G.-J., Chen, C.-H., & Chen, J.-P. (2015). Modulation of bone-specific tissue regeneration by incorporating bone morphogenetic protein and controlling the shell thickness of silk fibroin/chitosan/nanohydroxyapatite core-shell nanofibrous membranes. *ACS Applied Materials & Interfaces, 7*, 21170–21181.

Sultana, T., Hossain, M., Rahaman, S., Kim, Y. S., Gwon, J.-G., & Lee, B.-T. (2021). Multi-functional nanocellulose-chitosan dressing loaded with antibacterial lawsone for rapid hemostasis and cutaneous wound healing. *Carbohydrate Polymers, 272*, Article 118482.

Tan, J., Huang, L., Chen, X., Huang, Y., Ai, T., Li, D., Feng, Y., Hu, C., & Xie, Y. (2020). Osteoimmunomodulatory effects of biomaterial modification strategies on macrophage polarization and bone regeneration. *Regenerative Biomaterials, 7*, 233–245.

Tanaka, T., Narazaki, M., & Kishimoto, T. (2014). IL-6 in inflammation, immunity, and disease. *Cold Spring Harbor Perspectives in Biology, 6*, Article a016295-a016295.

Tang, W., Li, Y., Osimiri, L., & Zhang, C. (2011). Osteoblast-specific transcription factor osterix (Osx) is an upstream regulator of Satb2 during bone formation. *Journal of Biological Chemistry, 286*, 32995–33002.

Truby, R. L., & Lewis, J. A. (2016). Printing soft matter in three dimensions. *Nature, 540*, 371–378.

Vasconcelos, D. P., Costa, M., Amaral, I. F., Barbosa, M. A., Águas, A. P., & Barbosa, J. N. (2015). Modulation of the inflammatory response to chitosan through M2 macrophage polarization using pro-resolution mediators. *Biomaterials, 37*, 116–123.

Wan, Y., Wu, H., Cao, X., & Dalai, S. (2008). Compressive mechanical properties and biodegradability of porous poly(caprolactone)/chitosan scaffolds. *Polymer Degradation and Stability, 93*, 1736–1741.

Wang, C., Lin, K., Chang, J., & Sun, J. (2013). Osteogenesis and angiogenesis induced by porous β-CaSiO3/PDLGA composite scaffold via activation of AMPK/ERK1/2 and PI3K/Akt pathways. *Biomaterials, 34*, 64–77.

Wang, L., Qiu, Y., Lv, H., Si, Y., Liu, L., Zhang, Q., Cao, J., Yu, J., Li, X., & Ding, B. (2019). 3D superelastic scaffolds constructed from flexible inorganic nanofibers with self-fitting capability and tailorable gradient for bone regeneration. *Advanced Functional Materials, 29*, 1901407.

Wang, L. X., Zhang, S. X., Wu, H. J., Rong, X. L., & Guo, J. (2018). M2b macrophage polarization and its roles in diseases. *Journal of Leukocyte Biology, 106*, 345–358.

Wu, C., Chen, Z., Wu, Q., Yi, D., Friis, T., Zheng, X., Chang, J., Jiang, X., & Xiao, Y. (2015). Clinoenstatite coatings have high bonding strength, bioactive ion release, and osteoimmunomodulatory effects that enhance in vivo osseointegration. *Biomaterials, 71*, 35–47.

Wu, J., Zheng, K., Huang, X., Liu, J., Liu, H., Boccaccini, A. R., Wan, Y., Guo, X., & Shao, Z. (2019). Thermally triggered injectable chitosan/silk fibroin/bioactive glass nanoparticle hydrogels for in-situ bone formation in rat calvarial bone defects. *Acta Biomaterialia, 91*, 60–71.

Xiang, G., Liu, K., Wang, T., Hu, X., Wang, J., Gao, Z., Lei, W., Feng, Y., & Tao, T. H. (2020). In situ regulation of macrophage polarization to enhance osseointegration under diabetic conditions using injectable silk/sitagliptin gel scaffolds. *Advanced Science, 8*, Article 2002328.

Yang, X., Bakaic, E., Hoare, T., & Cranston, E. D. (2013). Injectable polysaccharide hydrogels reinforced with cellulose nanocrystals: Morphology, rheology, degradation, and cytotoxicity. *Biomacromolecules, 14*, 4447–4455.

Zhang, J., Allardyce, B. J., Rajkhowa, R., Zhao, Y., Dilley, R. J., Redmond, S. L., Wang, X., & Liu, X. (2018). 3D printing of silk particle-reinforced chitosan hydrogel structures and their properties. *ACS Biomaterials Science & Engineering, 4*, 3036–3046.

Zhang, X.-Y., Chen, Y.-P., Han, J., Mo, J., Dong, P.-F., Zhuo, Y.-H., & Feng, Y. (2019a). Biocompatiable silk fibroin/carboxymethyl chitosan/strontium substituted hydroxyapatite/cellulose nanocrystal composite scaffolds for bone tissue engineering. *International Journal of Biological Macromolecules, 136*, 1247–1257.

Zhang, X., Wang, C., Liao, M., Dai, L., Tang, Y., Zhang, H., Coates, P., Sefat, F., Zheng, L., Song, J., et al. (2019b). Aligned electrospun cellulose scaffolds coated with rhBMP-2 for both in vitro and in vivo bone tissue engineering. *Carbohydrate Polymers, 213*, 27–38.

Zhang, Y., Liu, X., Zeng, L., Zhang, J., Zuo, J., Zou, J., Ding, J., & Chen, X. (2019c). Polymer fiber scaffolds for bone and cartilage tissue engineering. *Advanced Functional Materials, 29*, 1903279.

Zhang, Z., Jiang, T., Ma, K., Cai, X., Zhou, Y., & Wang, Y. (2011). Low temperature electrophoretic deposition of porous chitosan/silk fibroin composite coating for titanium biofunctionalization. *Journal of Materials Chemistry, 21*, 7705.

Zheng, G., Liu, X., Wang, X., Chen, L., Xie, H., Wang, F., Zheng, H., Yu, W., & Ma, X. (2014). Improving stability and biocompatibility of alginate/chitosan microcapsule by fabricating bi-functional membrane. *Macromolecular Bioscience, 14*, 655–666.

Zhong, J., Wu, X., Wang, Y., Li, M., Li, Y., Liu, X., Zhang, X., Lan, Z., Wang, J., Du, Y., et al. (2021). Zn/Sr dual ions-collagen co-assembly hydroxyapatite enhances bone regeneration through procedural osteo-immunomodulation and osteogenesis. *Bioactive Materials, 10*, 195–206.

Zhou, C., Shi, Q., Guo, W., Terrell, L., Qureshi, A. T., Hayes, D. J., & Wu, Q. (2013). Electrospun bio-nanocomposite scaffolds for bone tissue engineering by cellulose nanocrystals reinforcing maleic anhydride grafted PLA. *ACS Applied Materials & Interfaces, 5*, 3847–3854.

Zhou, M., Wu, X., Luo, J., Yang, G., Lu, Y., Lin, S., Jiang, F., Zhang, W., & Jiang, X. (2021). Copper peptide-incorporated 3D-printed silk-based scaffolds promote vascularized bone regeneration. *Chemical Engineering Journal, 422*, Article 130147.